Supporting information

Phase Shuttle Enhanced Electrochemical Ozone Production

Jia Liu[1,#], Shibin Wang[1,#], Zhangnv Yang[5,#], Chencheng Dai[2, #], Ge Feng[1], Beibei Wu[5], Wenwen Li[1], Lu Shu[1], Kamal Elouarzaki[2,3,4], Xiao Hu[2,4], Xiaonian Li[1],Hui Wang[6], Zhen Wang[5,*], Xing Zhong[1,*], Zhichuan J. Xu[2,3*], & Jianguo Wang[1*]

[1]Institute of Industrial Catalysis, State Key Laboratory Breeding Base of Green-Chemical Synthesis Technology, College of Chemical Engineering, Zhejiang University of Technology, Hangzhou 310032, P.R. China.

[2]School of Materials Science and Engineering, Nanyang Technological University, 50 Nanyang Avenue, Singapore 639798, Singapore.

[3]Center for Advanced Catalysis Science and Technology, Nanyang Technological University, 50 Nanyang Avenue, Singapore 639798, Singapore.

[4]Nanyang Environment and Water Research Institute (NEWRI), Nanyang Technological University, 1 Cleantech Loop, CleanTech One, 637141 Singapore

[5]Key Lab of Vaccine, Prevention and Control of Infectious Disease of Zhejiang Province, Zhejiang Provincial Center for Disease Control and Prevention, Hangzhou 310015, China.

[6]Women's Hospital, School of Medicine, Zhejiang University, Hangzhou, Zhejiang, China.

Supporting files

Method: 8

Supporting Figures: 60

Supporting Tables: 9

Method

1. Materials

Commercial β-PbO_2 (≥ 97%)(Merck), Commercial Pb_3O_4 (≥ 98%)(Jiuding Chemical), Ethanol (≥99.7%, Sinopharm Chemical Reagent Co., Ltd), HNO_3 (AR, 65-68%, Sinopharm Chemical Reagent Co., Ltd), Propanone (AR, ≥99.5%, Sinopharm Chemical Reagent Co., Ltd), K_2SO_4 (99%, Aladdin Industrial Co., Ltd.), Nafion PFSA polymer (5.0-5.4 wt %; Suzhou Yilongcheng Energy Technology Co., Ltd.), carbon fiber (CF; CeTech Co., Ltd.), K_2SO_4 (99%, Aladdin Industrial Co., Ltd.), $H_2{}^{18}O$(Heowns), Pt/C (20% Pt) (Shanghai Hesen Electric Co., Ltd.), and Millipore deionized water were used to prepare all the solutions.

2. Characterizations

Transmission electron microscopy (TEM) images were obtained using TecnaiG2 F30 S-Twin at a 300 kV acceleration voltage. Using X'Pert PRO, the crystal structures of the samples were primarily characterized by X-ray diffraction (XRD). The Raman spectra were acquired by a Horiba XploRA Raman spectrometer equipped with a 50× objective and 25mW 633 nm laser. The C 1s peak was identified at 284.5eV as an internal standard, and X-ray photoelectron spectroscopy (XPS) was done using Kratos AXIS Ultra DLD equipment with 300 W Al-K radiation. XAS experiments were performed at the Singapore Synchrotron Light Source, XAFCA beamline. Data analysis was performed with the Athena software package. The Pb foil, PbO, Pb_3O_4, and β-PbO_2 were used as reference samples to determine Pb valence in XANES analysis (Supplementary Figure 30) [1, 2].

3. Electrode preparation

Firstly, Carbon Cloth (CC) was cut into pieces of 2 cm × 2 cm, and then it was ultrasonically processed in HNO_3 (40 wt%), acetone, ethanol, and deionized water separately for 30 min. After that, the CC was dried for 24 h in a vacuum at 60 °C. In 900 μL of ethanol and 100 μL of Nafion solution, 8 mg of electrocatalyst was dispersed by ultrasonication. After being dropped slowly onto the CC (catalyst mass loading of 2 mg/cm^2), the electrocatalyst was dried under infrared light.

4. Electrochemical measurements

The electrochemical oxidation of water was first studied by voltammetry measurement performed by a CHI 760E electrochemical workstation employing the standard three-electrode system. The as-prepared CC electrode with electrocatalyst (PbO_X/CC), Ag/AgCl (saturated KCl), and platinum sheet served as the working, reference, and counter electrodes, respectively (as shown in Figure S1). The catalyst was first pretreated by 20 consecutive cyclic voltammetry (CV) scans with a scan rate of 10 mV/s in the potential range of 0 to 3 V vs. Ag/AgCl (saturated KCl). The linear sweep voltammetry (*LSV)* was later conducted in the same potential range with a scan rate of 1 mV/s. All the CV and LSV tests were performed in the saturated K_2SO_4 solution at room temperature, with 85%-iR compensation applied. All potentials applied are converted the potentials into the reversible hydrogen electrode (RHE) in the figures using the equation $E\ (RHE) = E\ (Ag/AgCl) + 0.059 \times pH + 0.197$. All the experiments were carried out using deionized water (18.2 MΩ, HHitech).

The electrochemical active surface area (ECSA) was obtained through the double-layer capacitance (C_{dl}) measurement. First, the C_{dl} of electrodes was measured via CV tests in saturated K_2SO_4 electrolyte. The CVs were conducted in the potential range of 0.6 – 0.8 V vs. RHE, with scan rates of 20, 40, 60, 80, 100, and 120 mV s^{-1}. The ESCA is then calculated based on the obtained C_{dl} assuming the specific C_{dl} of a smooth metal surface 60 μF cm^{-2}.

5. Electrochemical ozone generation and product analysis

The EOP MEA electrolyzer was assembled using a Nafion membrane coated with lead oxides (β-PbO_2, Pb_3O_4) and Pt/C on each side as the working and counter electrodes, respectively. An Ag/AgCl (3 M KCl) reference electrode was placed in the analyte chamber. The ultrapure water was flown through the MEA electrolyzer as the electrolyte (both analyte and catholyte). An Ozone Analyzer (UVIZ-1200) was used to measure gaseous ozone concentration (g/m^3). The flow rate of gaseous ozone was measured by a soap film flowmeter (L/min). The gaseous ozone production rate (Q, kg/h) can be calculated and further used for faradaic efficiency calculation. The faradaic efficiencies of gaseous ozone were tested at different constant current densities in the EOP MEA electrolyzer. The current density was controlled by the galvanostat

(Henghui, HLR-1820HD), and the corresponding anode potential was detected by the external potentiometer (CorrTest, CS1002). The faraday efficiency of gaseous ozone evolution is calculated based on the equation below:

$$FE = \frac{5 \times F \times Q}{3 \times M \times I}$$

Where M stands for the molecular weight of O_3 (48), I is the current (A), F is the Faraday's constant (9.6485 × 10^4 C/mol), and Q is the O_3 production rate (kg/h).

6. Inactivation of SARS-CoV-2 by ozonated water

The ozonated water was obtained from bubbling EOP electrolyzer-generated ozone gas into quantitative normal saline (15 mL) at ambient temperature and pressure. The device to prepare ozonated water is shown in Supplementary Fig. 41. Subsequently, the ozonated water was used to inactivate SARS-CoV-2 suspended in liquid solutions (Minimum Essential Medium (MEM)). During the inactivation process of ozone liquid solution, 500 μL of MEM virus solution (5.6×10^6 $TCID_{50}$/mL) was mixed with 500 μL of ozonated water or normal saline (control) and was left to react before being titrated, and plaques counted. The control reaction times were 30 s, 1 min, 3 min, 5 min, and 10 min, respectively. To neutralize the remaining ozone after inactivation, $Na_2S_2O_3$ (0.01 M, 21 μL) was added as a neutralizer. The inactivated solution was then serially diluted 10-fold to infect Vero cells grown in monolayers in 96-well plates for 1 h (Supplementary Fig. 42). The cells were then overlaid with MEM containing 3% FBS and incubated for 72 h. Afterward, the cytopathic effect (CPE) was observed, and the virus titer was calculated according to the Reed-Muench method.

7. In situ differential electrochemical mass spectra (DEMS)

DEMS measurements were carried out to determine the ^{18}O-labeled volatile reaction products of Commercial Pb_3O_4 electrocatalysts during OER and EOP process using a QAS 100 device (Linglu Instruments, Shanghai). The quadrupole mass spectrometer (Pfeiffer Prisma) was used in the main chamber to analyze the gaseous products. A porous PTFE membrane separated the electrolytic chamber from the main chamber. K_2SO_4 was dissolved in $H_2{}^{18}O$ rather than deionized water, and the solution then served as the electrolyte (2.4 V *vs.*RHE) for the electrolysis. The reference electrode and counter electrode were an Ag/AgCl electrode and a Pt wire, respectively. By sputtering

Au onto PTFE films 50 μm thick, the working electrodes were prepared and positioned at the bottom of the electrolyte to directly introduce gaseous products to the main chamber. Then, the electrocatalysts were dropped and cast onto the Au with a loading mass of 0.5 mg/cm^{-2}. CHI 760 was used to conduct electrolysis experiments with constant voltage. Monitoring the values of m/z signals of 32, 34, and 36 allowed the determination of the O_2 species, while monitoring the values of 48, 50, 52, and 54 allowed the determination of the O_3 species.

8. DFT Calculation Method

Structural optimizations of the PbO_2 (101), PbO_2 (110), PbO (010), PbO (111), Pb_3O_4 (110), and Pb_3O_4 (211) surface were calculated using Vienna ab initio simulation package (VASP)[3, 4]. The exchange-correlation function of Perdew-Burke-Ernzerhof (PBE)[5] and the projected augmented wave (PAW) method[6, 7] was used to describe the ion-electron interaction. The cutoff energy for the plane-wave basis sets was 400 eV. The O 2s2p and Pb 6s6p5d electrons are treated as valence states. The geometry and energy convergence criteria were set to be 0.02 eV/Å and 10^{-6} eV, respectively. For the above surfaces, a vacuum space of 15 Å was added to the z-direction of the slab modules.

For the pH-potential phase diagram of the β-PbO_2(101) surface and the Pb_3O_4(110) surface, the calculations were performed by adding different amounts of charges into the cell to model the systems with a range of electrode potentials from 0.9 V to 2.0 V vs. SHE. The solvation environment was included by applying the implicit solvation model VASPsol[8] based on solving the linearized Poisson–Boltzmann equation. The dielectric constant of water was set to a relative permittivity of 78.4, and the surface tension was set to zero.

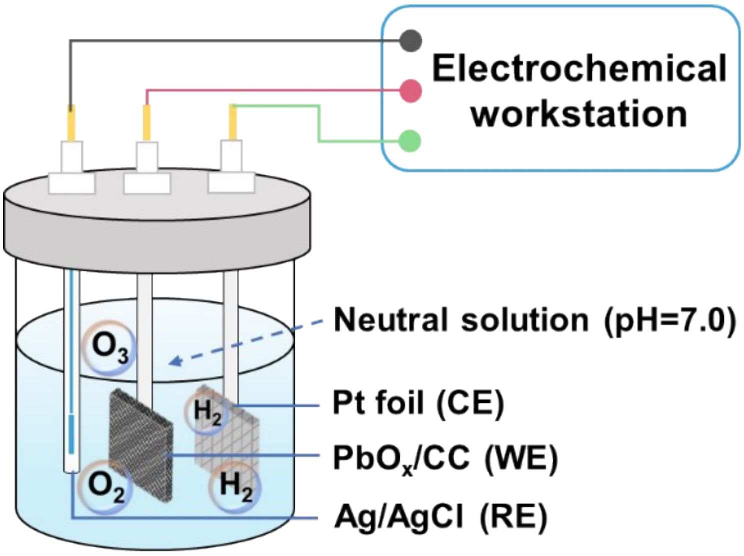

Figure S1. Schematic diagram of a single electrolytic cell.

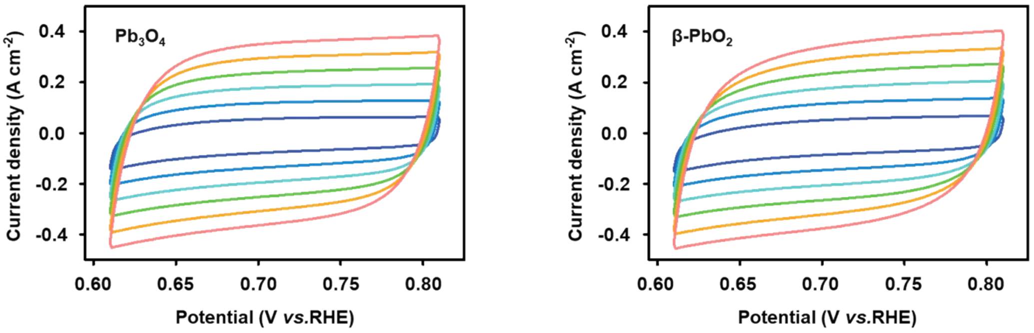

Figure S2. Cyclic voltammetry curves at various scan rates of 20, 40, 60, 80, 100, and 120 mV s^{-1} in saturated K_2SO_4 solution of Pb_3O_4 and β-PbO_2 for the determination of double-layer capacitance.

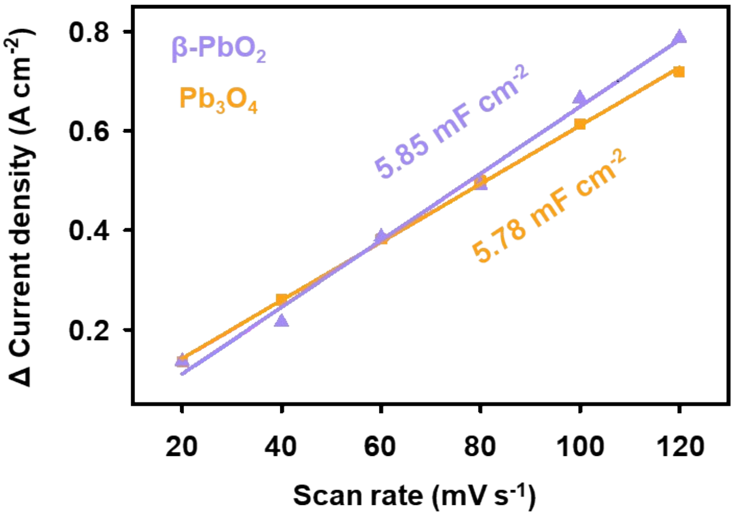

Figure S3. Different scan rates to measure capacitive currents for Pb_3O_4 and β-PbO_2.

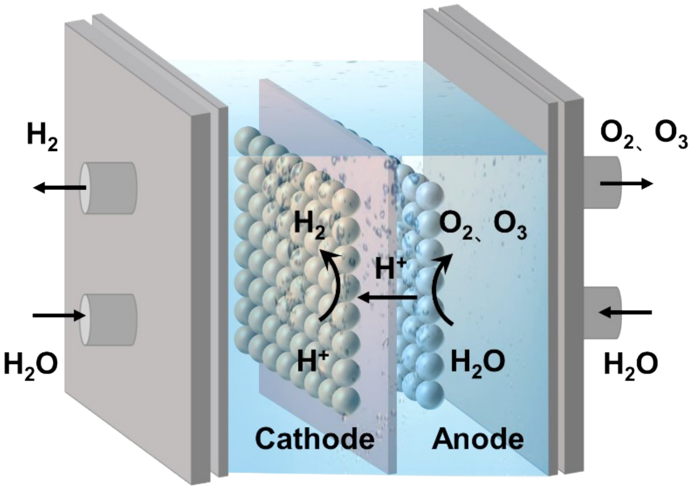

Figure S4. Schematic illustration of the EOP electrolyzer.

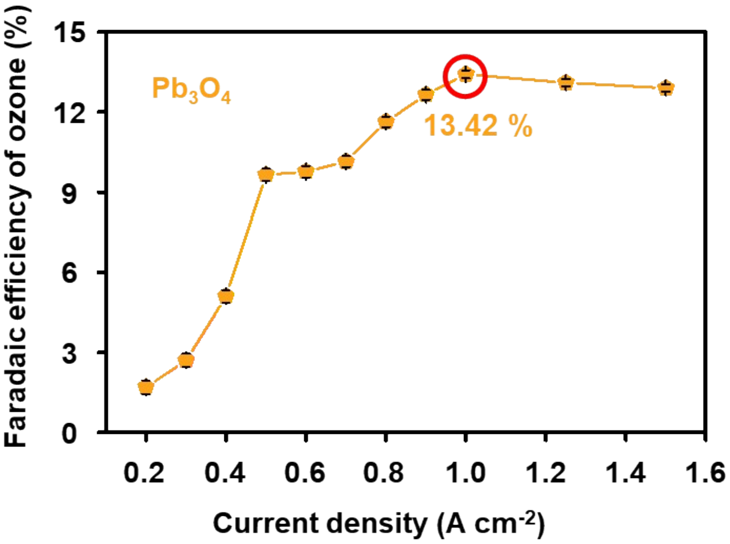

Figure S5. The faradaic efficiency of ozone for commercial Pb_3O_4 at different constant current densities of 0.2-1.5 A cm^{-2} using the EOP electrolyzer.

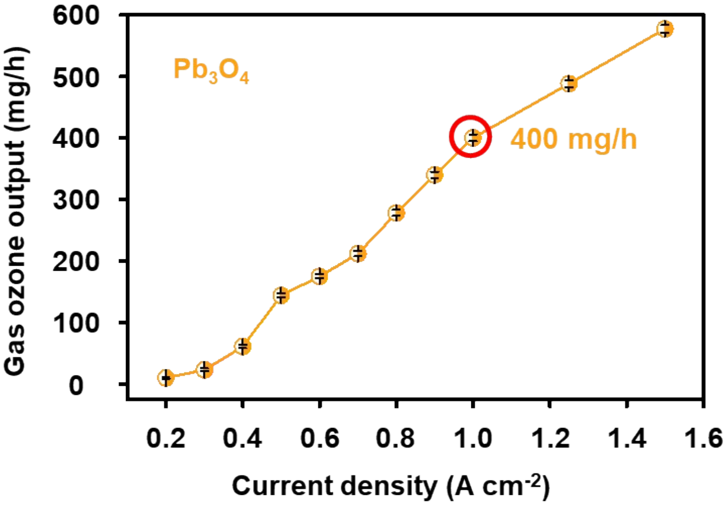

Figure S6. The gas ozone output for the EOP electrolyzer with the anode of the Pb_3O_4 at a constant current density of 0.2-1.5 A cm^{-2}.

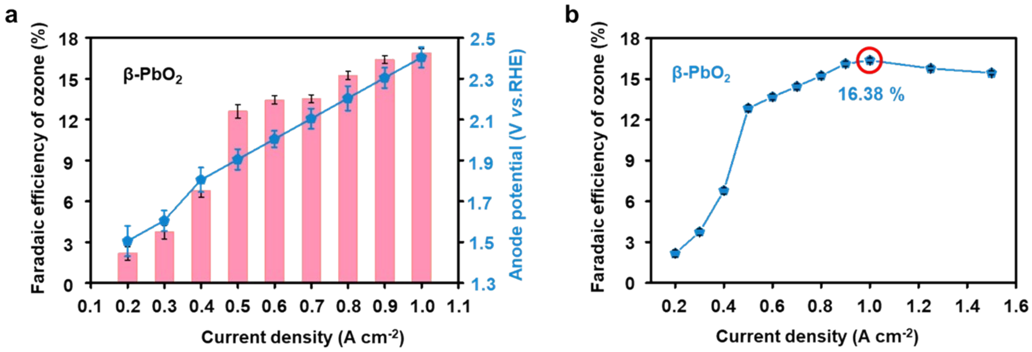

Figure S7. (a) The faradaic efficiency towards ozone generation for the β-PbO$_2$ at different applied current densities using the EOP MEA electrolyzer. (b) The Faradaic efficiency of ozone for commercial β-PbO$_2$ at different constant current densities of 0.2-1.5 A cm^{-2} using the EOP electrolyzer.

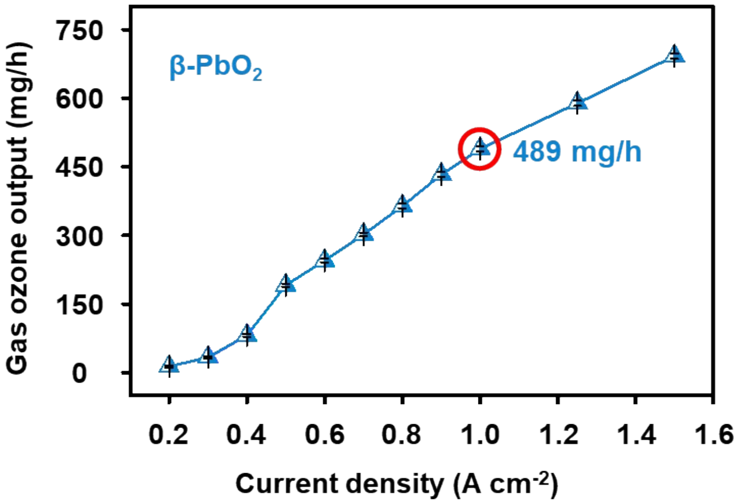

Figure S8. The gas ozone output for the EOP electrolyzer with the anode of β-PbO_2 at a constant current density of 0.2-1.5 A cm^{-2}.

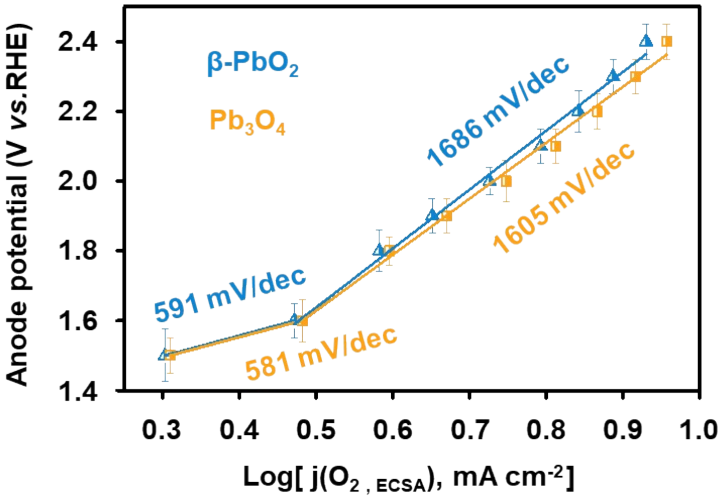

Figure S9. Tafel plot of the partial O_2 current densities normalized electrochemically active surface area of commercial Pb_3O_4 based on the EOP electrolyzer.

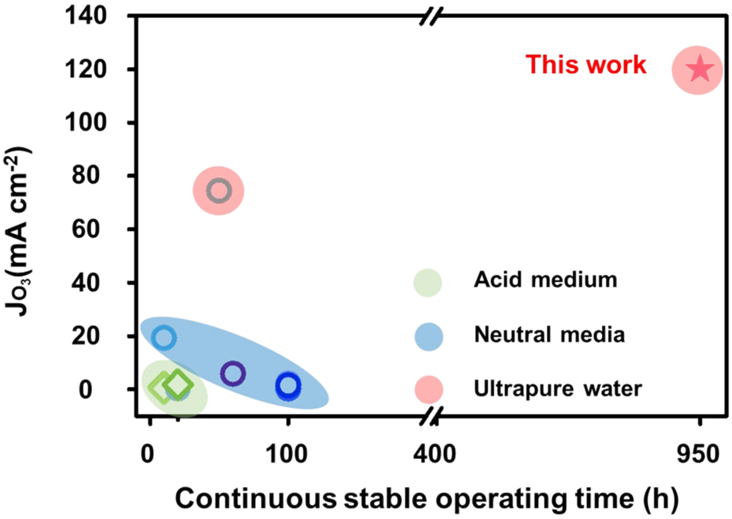

Figure S10. EOP performance comparison of different electrocatalysts (based on continuous stable operation time and ozone partial current density).

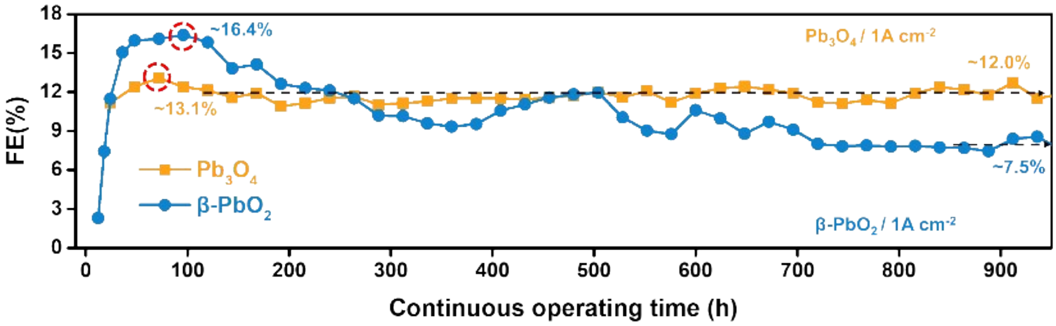

Figure S11. Faradaic efficiency of the EOP electrolyzer with an anode of commercial Pb_3O_4 and β-PbO_2 for 950 h at the constant current condition of 1.0 A cm^{-2}.

Figure S12. The schematic illustration of the complete reconstruction of Pb_3O_4 before and after the EOP process at the constant current condition of 1.0 A/cm^2 (anode potential was between 2.40 to 2.45 V *vs.*RHE).

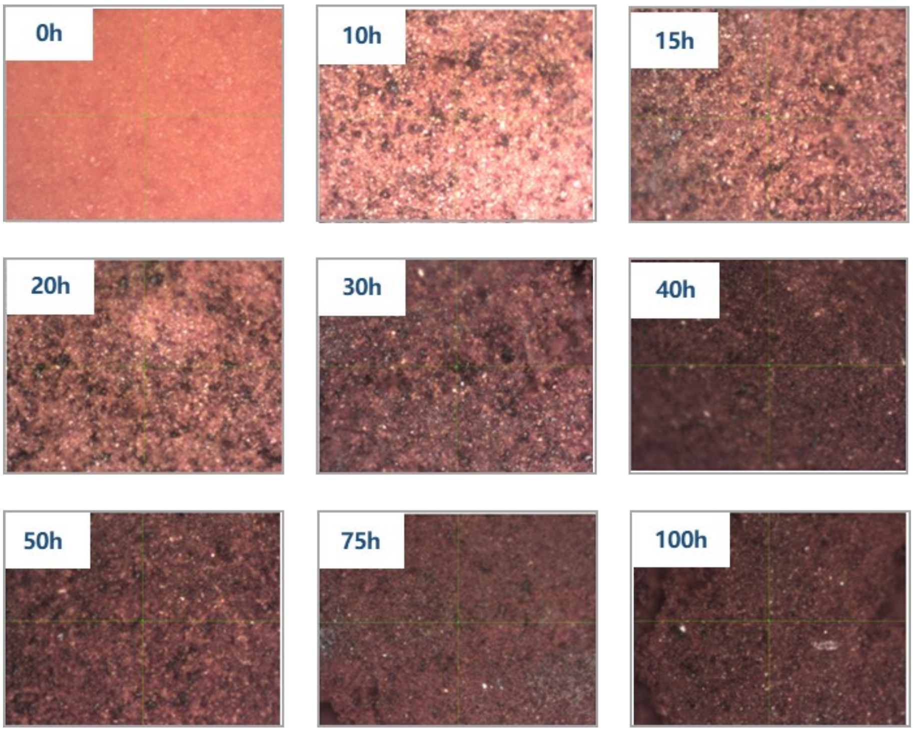

Figure S13. 50x images based on Pb_3O_4 before and after the EOP process at the high current of 1.0 A cm^{-2} (anode potential was between 2.40 to 2.45 V *vs.*RHE).

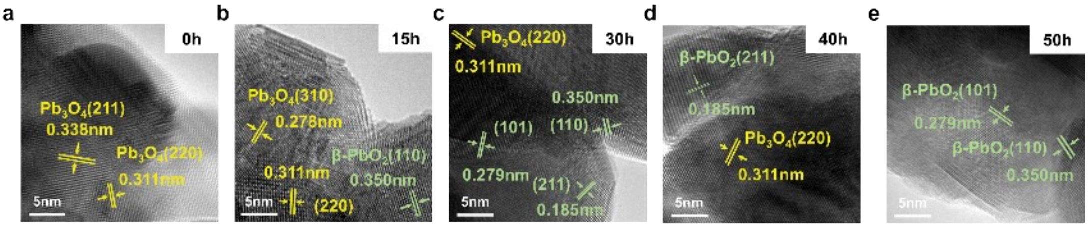

Figure S14. HRTEM images of Pb_3O_4 under different EOP durations from 0 h to 50 h.

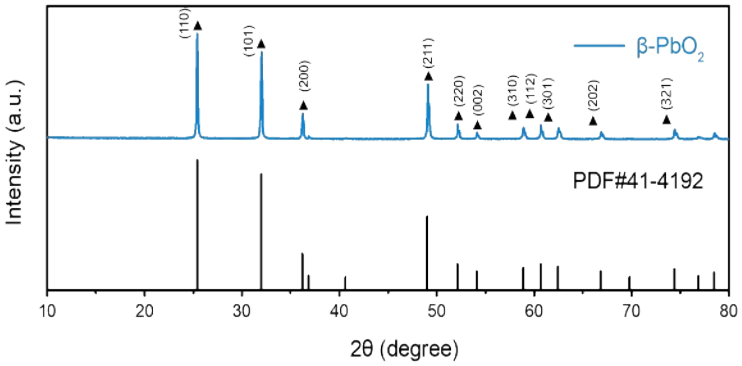

Figure S15. XRD patterns of commercial β-PbO_2 and the standard patterns of β-PbO_2 (PDF # 41-1492).

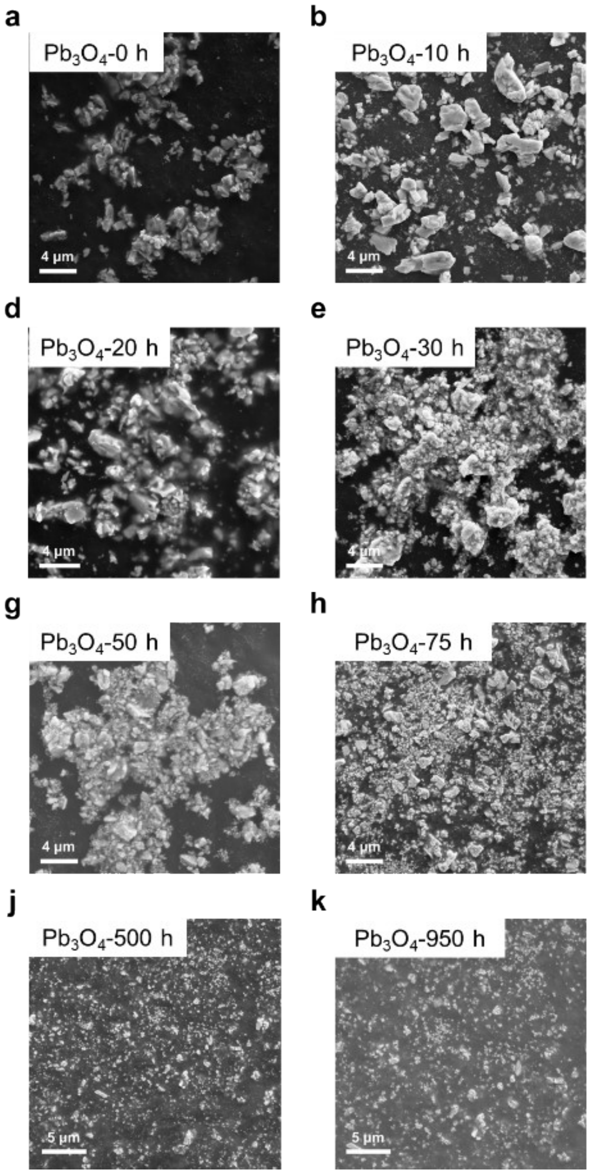

Figure S16. SEM images of Pb_3O_4 under different EOP durations at the high current of 1.0 A cm^{-2} (anode potential was between 2.40 to 2.45 V *vs.*RHE).

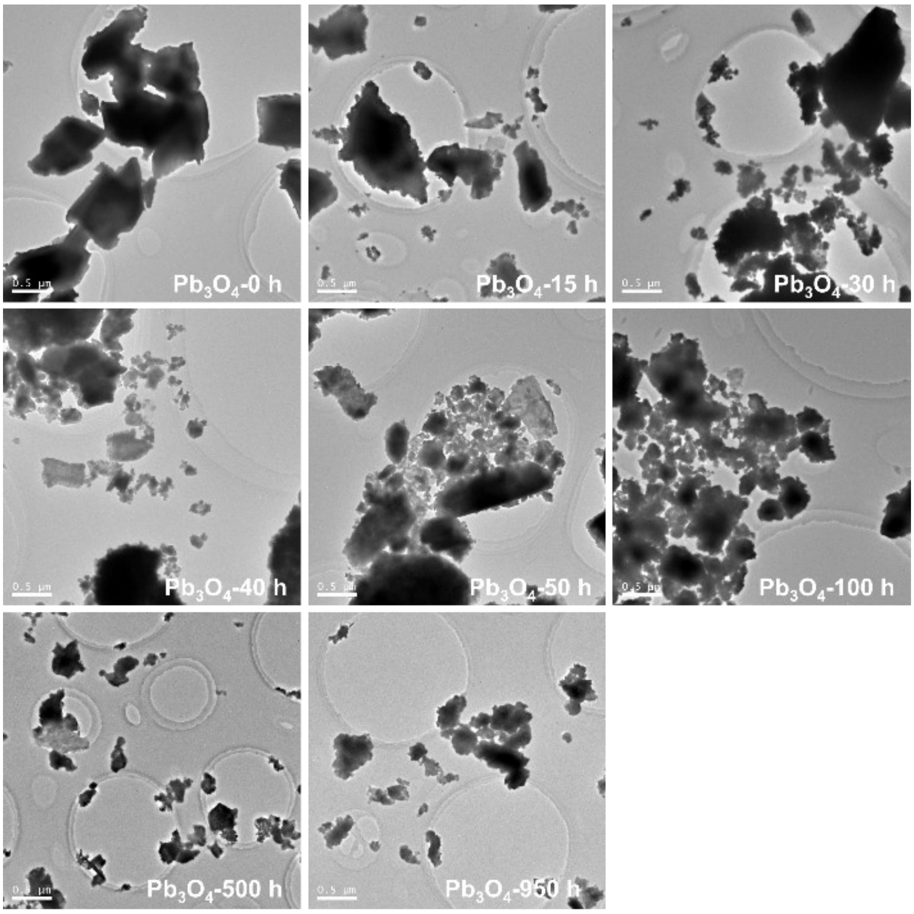

Figure S17. TEM images of Pb_3O_4 under different EOP durations at the high current of 1.0 A cm^{-2} (anode potential was between 2.40 to 2.45 V *vs.*RHE).

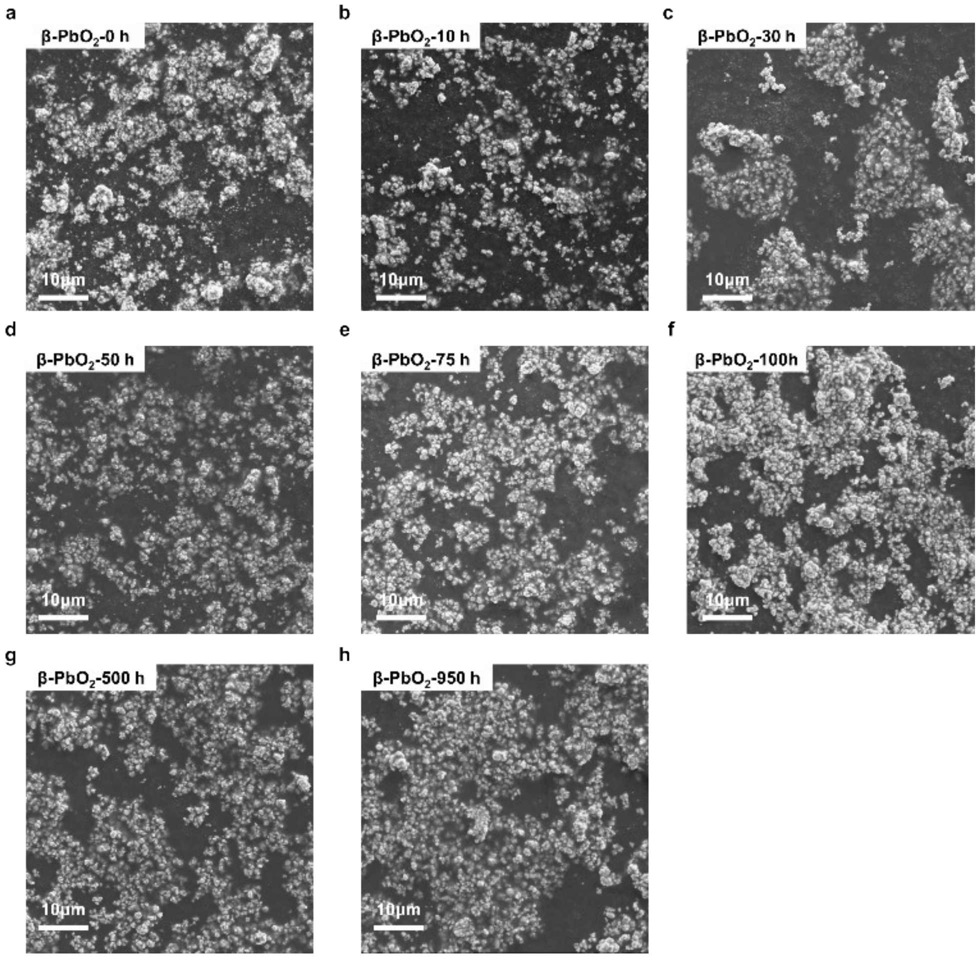

Figure S18. SEM images of β-PbO_2 under different EOP durations at the high current of 1.0 A cm^{-2} (anode potential was between 2.40 to 2.45 V *vs.*RHE).

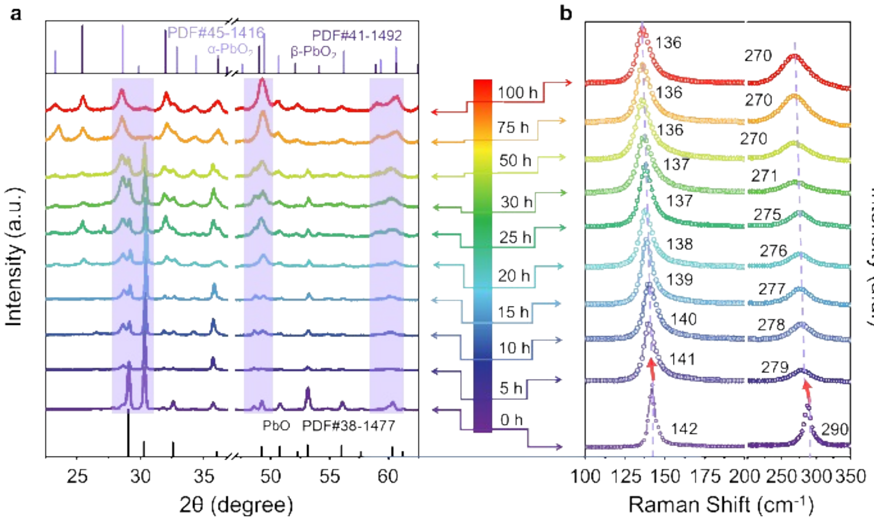

Figure S19. a, Ex situ XRD patterns, b, Ex situ Raman spectra based before and after EOP treatment in EOP electrolyzer at a high current of 1.0 A cm^{-2} (anode potential was between 2.40 to 2.45 V *vs.*RHE).

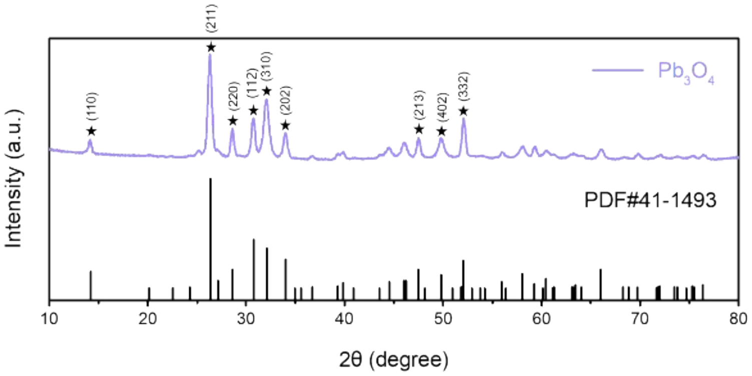

Figure S20. XRD patterns of commercial Pb_3O_4 and the standard patterns of Pb_3O_4 (PDF # 41-1493).

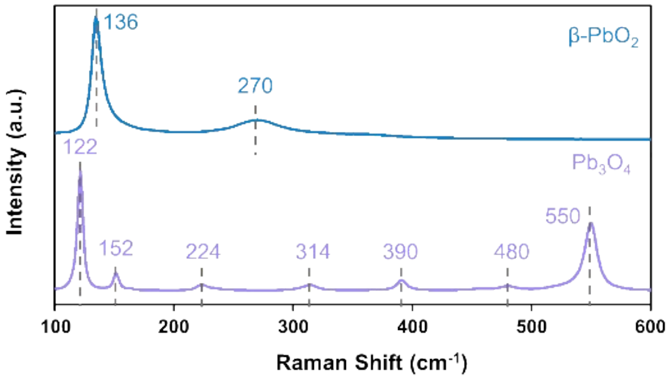

Figure S21. The Raman spectrum of commercial β-PbO_2 and Pb_3O_4.

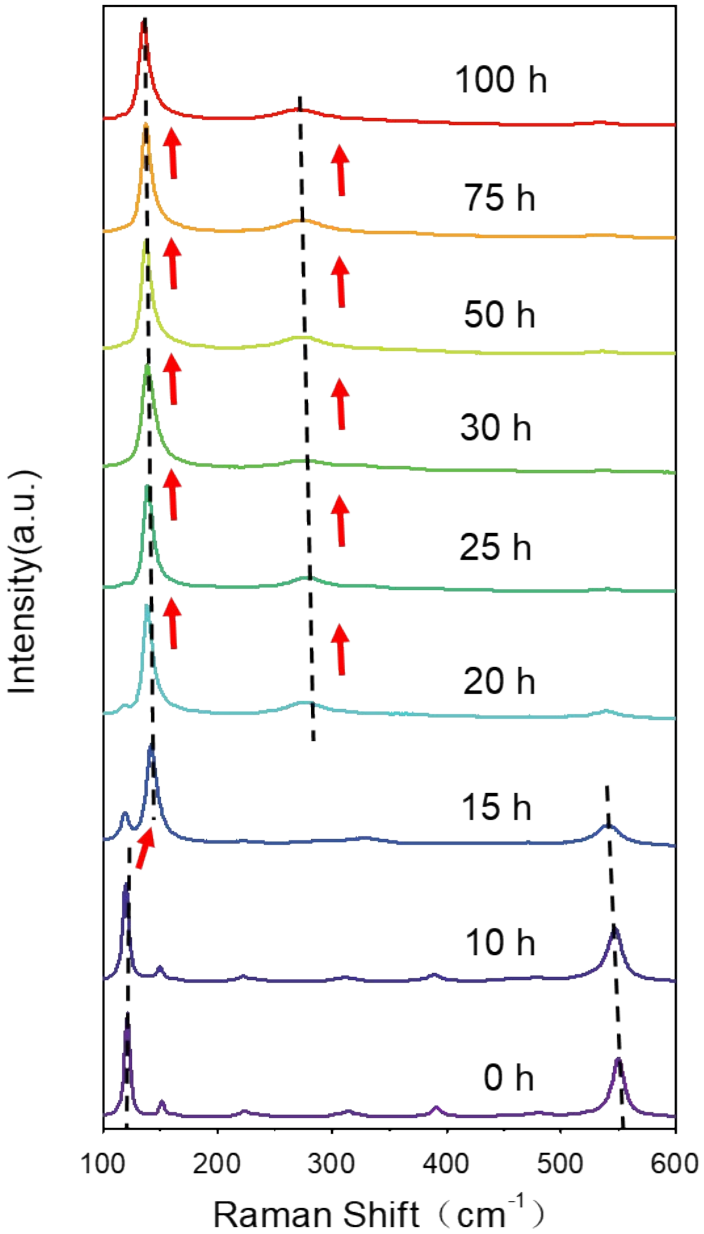

Figure S22. Ex situ Raman spectrum based Pb_3O_4 before and after the EOP process at the high current of 1.0 A cm^{-2} (anode potential was between 2.40 to 2.45 V *vs.*RHE).

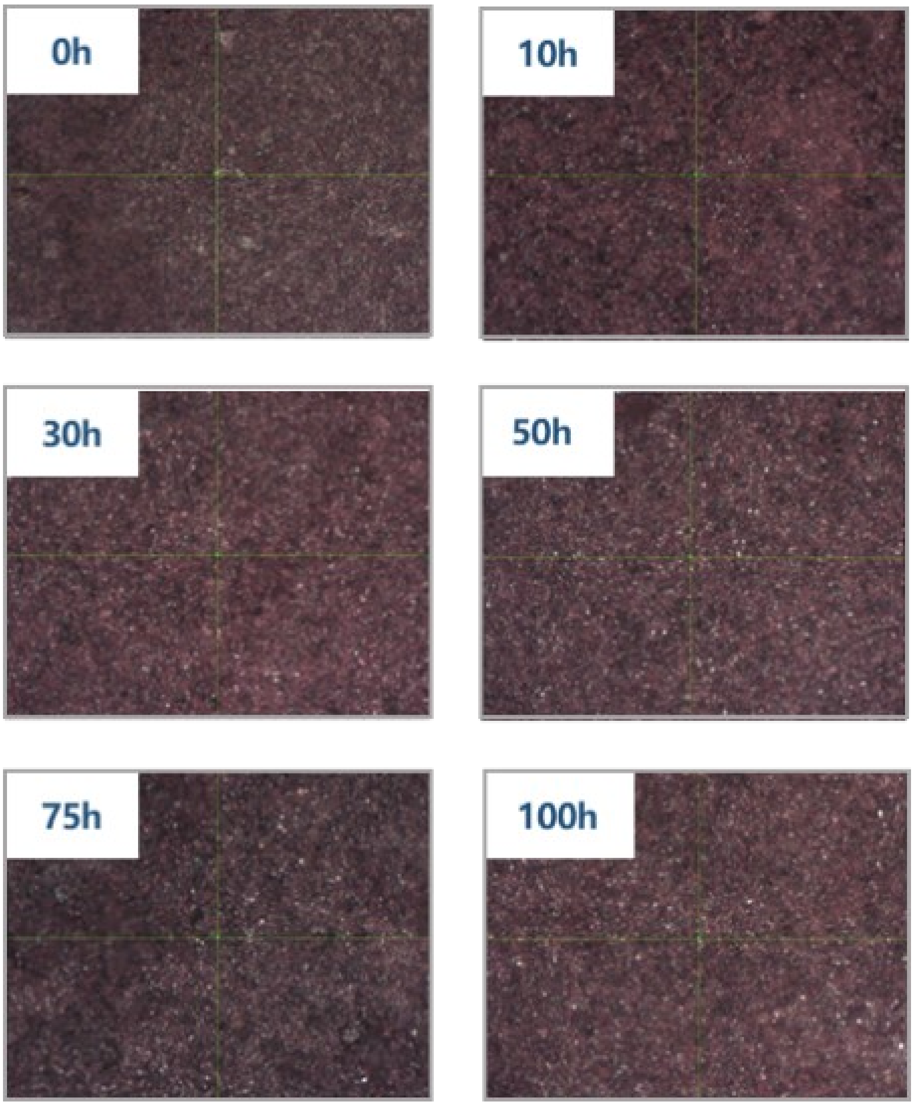

Figure S23. 50x images based on β-PbO_2 before and after the EOP process at the high current of 1.0 A cm^{-2} (anode potential was between 2.40 to 2.45 V *vs.*RHE).

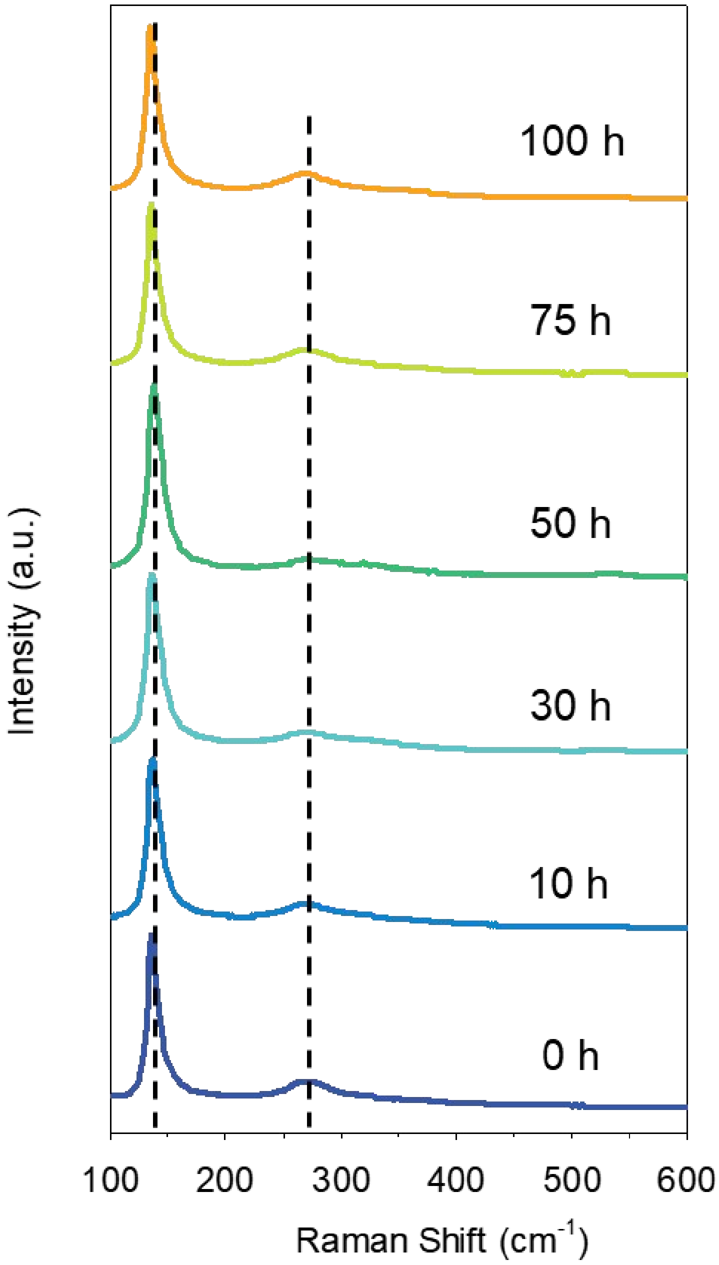

Figure S24. Ex situ Raman spectrum based β-PbO_2 before and after the EOP process at the high current of 1.0 A cm^{-2} (anode potential was between 2.40 to 2.45 V *vs.*RHE).

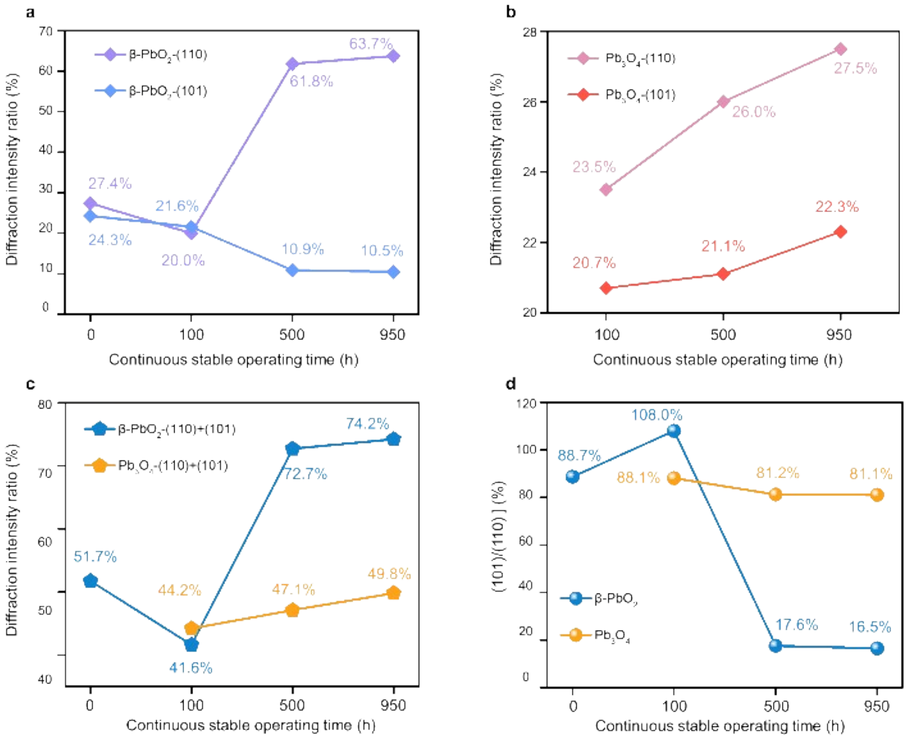

Figure S25. The change in the ratio of (101)/(110) crystal planes in Pb_3O_4 and β-PbO2 under different EOP durations.

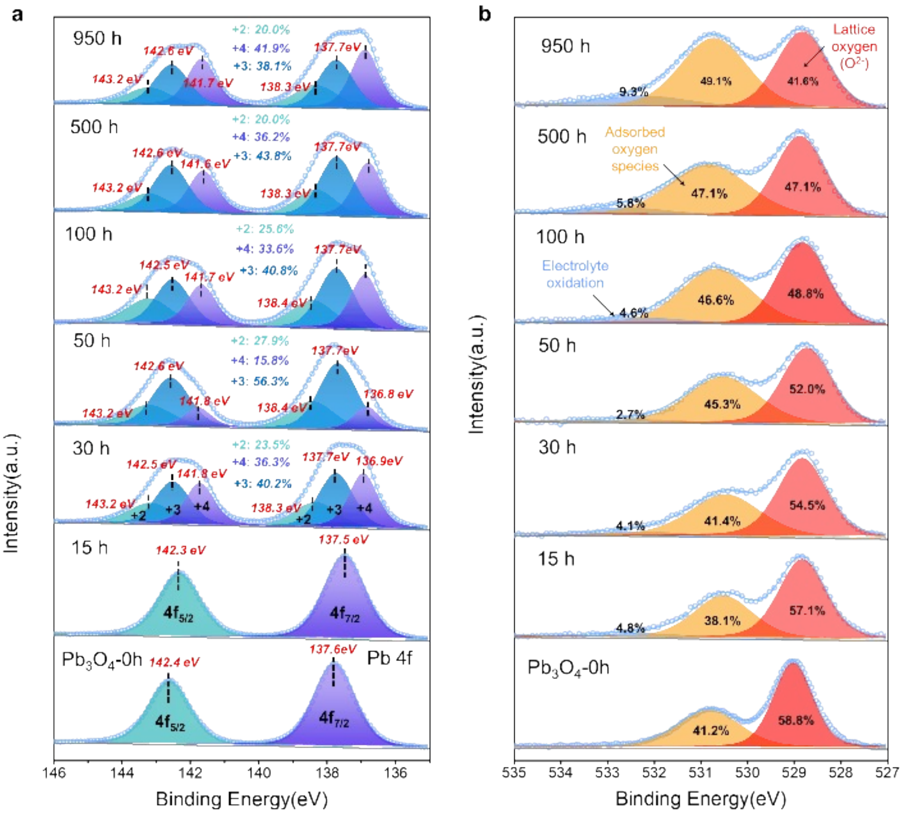

Figure S26. Pb 4f spectra, and e, O1s spectra of Pb_3O_4 based before and after EOP treatment in EOP electrolyzer at a high current of 1.0 A cm^{-2} (anode potential was between 2.40 to 2.45 V *vs.*RHE).

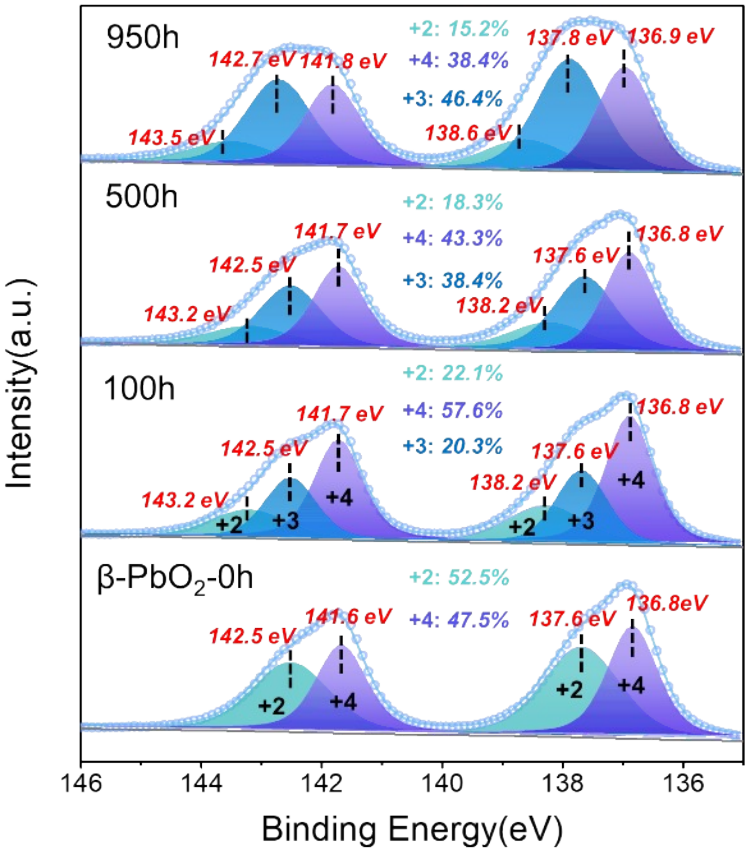

Figure S27. Pb 4f spectra of β-PbO_2 based before and after EOP treatment in EOP electrolyzer at a high current of 1.0 A cm^{-2} (anode potential was between 2.40 to 2.45 V *vs.*RHE).

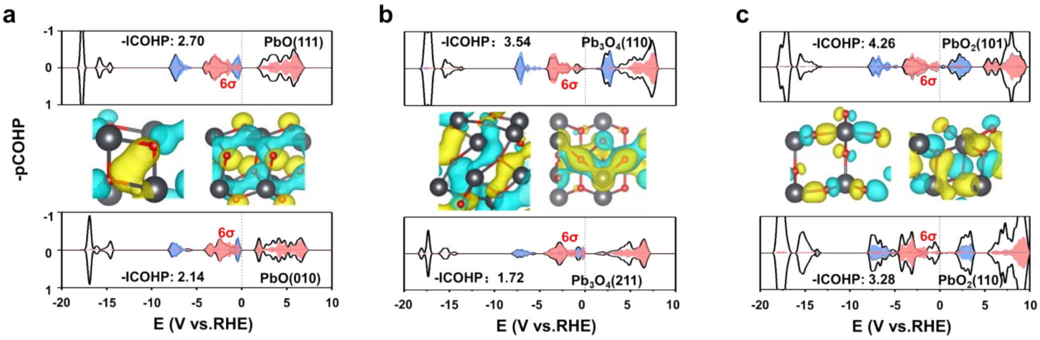

Figure S28. DFT calculated crystal orbital Hamilton population (COHP) as well as the Kohn-Sham orbital of the interaction below the Fermi level for the exposed Pb-O covalent bonds over the PbO (101), PbO (111), Pb_3O_4 (110), Pb_3O_4 (211), PbO_2 (101) and PbO_2 (110) surface, with blue and pink shadow indicating the covalent O_{2p}-Pb_{6s} and O_{2p}-Pb_{6s} interactions, respectively.

To elucidate the stability of the exposed lead oxide surfaces, COHP for the exposed Pb-O covalent bonds over the PbO_2 (101), PbO_2 (110), PbO (010), PbO (111), Pb_3O_4 (110), and Pb_3O_4 (211) surface, with the corresponding results shown in Figure 3g-i. Interestingly, the COHP results show that the Pb-O covalent interaction was mainly dominated by the interaction between Pb-2s/2p and O-2p orbital, the Pb-5d orbital was fulfilled and not responsible for the Pb-O covalent interaction[9]. Such Pb-O covalent interaction is not a typical one, which is usually dominated by d orbital and O-2p orbital[10]. The integrated COHP (ICOHP) value was calculated to be 4.26, 3.28, 2.14, 2.70, 3.54, and 1.72, respectively for the PbO_2 (101), PbO_2 (110), PbO (010), PbO (111), Pb_3O_4 (110), and Pb_3O_4 (211) surface. By comparing the ICOHP value of the Pb-O bond over different surfaces, it was possible to conclude that the PbO_2 surfaces exhibited the highest stability due to the strongest Pb-O covalent interaction. The Pb-O covalent interaction on different surfaces follows the order of PbO_2 (101) > Pb_3O_4 (110) > PbO_2 (110) > PbO (111) > PbO (010) > Pb_3O_4 (211). The Kohn-Sham orbital analysis was also applied to give an intuitive understanding of the Pb-O covalent interactions. As shown in Supplementary Figure 33, the covalent interaction between the Pb-6p and the O-2p orbital occupied the energy levels below the Fermi level, with the corresponding Kohn-Sham wave function orbital also shown in this figure. Note that for the above-mentioned lead oxide surfaces, the Pb-O was dominated by the σ covalent bond between the Pb-6p and the O-2p orbital.

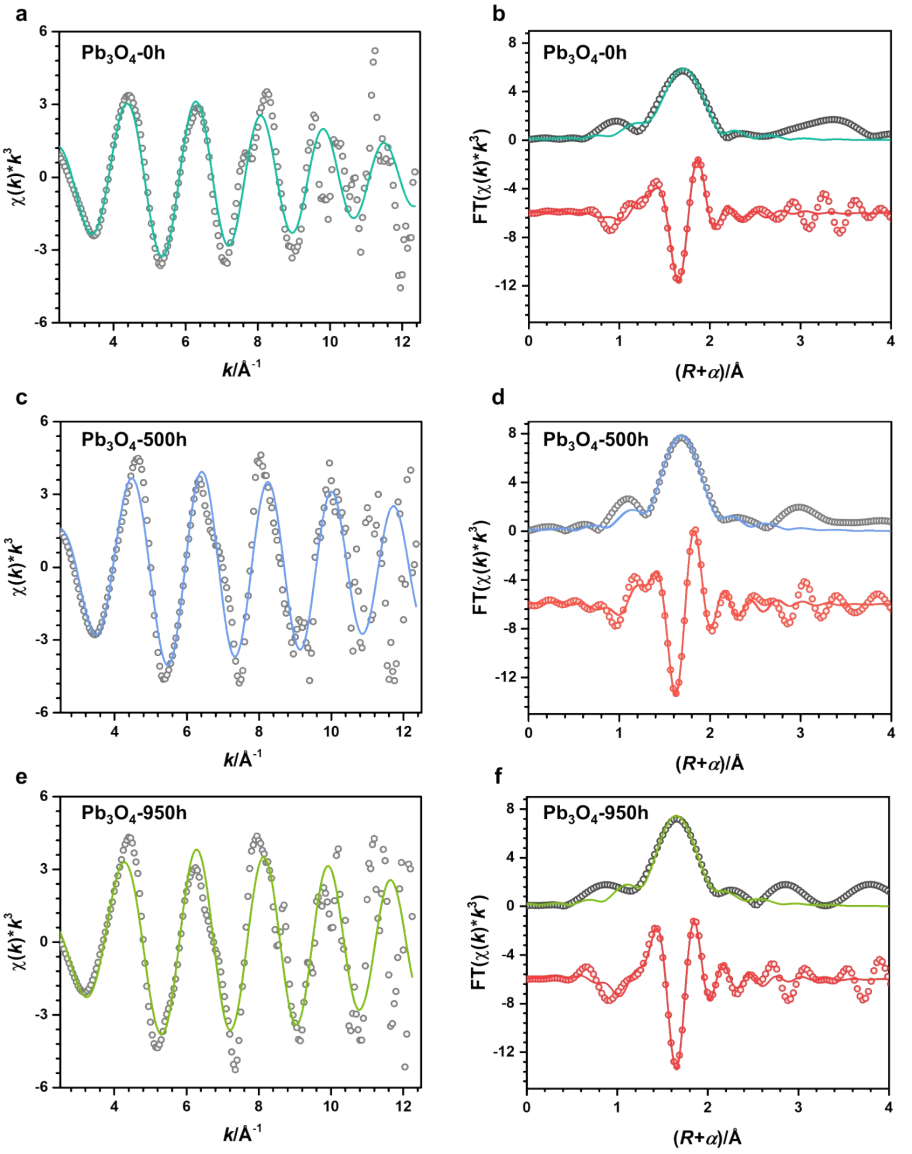

Figure S29. Pb L-edge EXAFS (points) and curve fits (lines) for Pb_3O_4-0h (a), Pb_3O_4-500h (c) and Pb_3O_4-950h (e), shown in k3-weighted k-space. Pb L-edge EXAFS (points) and curve fits (lines) for Pb_3O_4-0h (b), Pb_3O_4-500h (d), and Pb_3O_4-950h (f), shown in R-space (FT magnitude and imaginary part). Data are k3-weighted and uncorrected for phase.

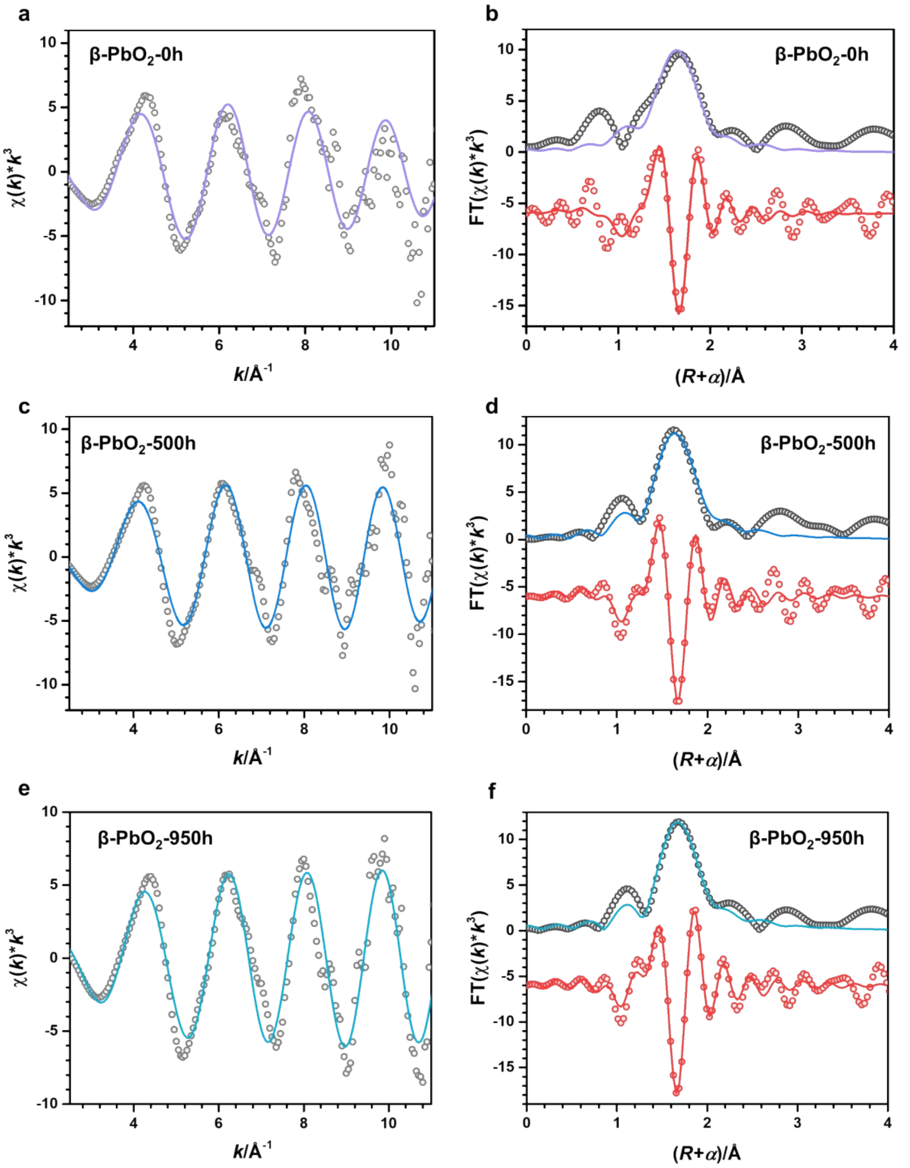

Figure S30. Pb L-edge EXAFS (points) and curve fits (lines) for β-PbO$_2$-0h (a), β-PbO$_2$-500h (c) and β-PbO$_2$-950h (e), shown in k3-weighted k-space. Pb L-edge EXAFS (points) and curve fits (lines) for β-PbO$_2$-0h (b), β-PbO$_2$-500h (d), and β-PbO$_2$-950h (f), shown in R-space (FT magnitude and imaginary part).

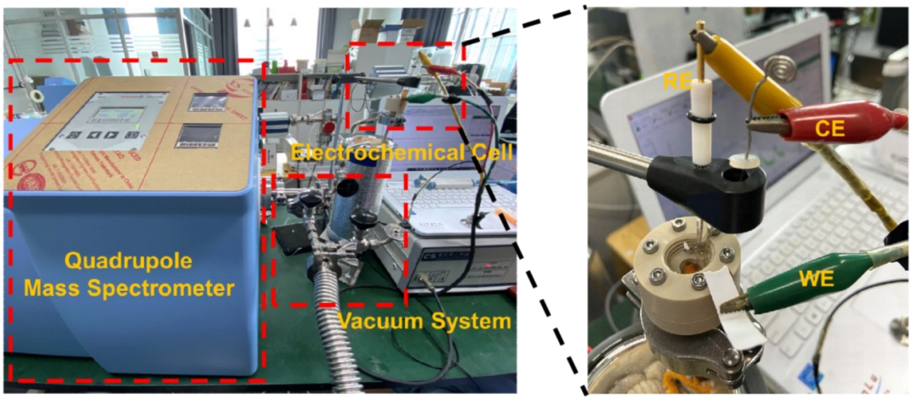

Figure S31. The photograph of the DEMS technique with mass spectra and the photograph of the electrolysis cell for DMES measurement.

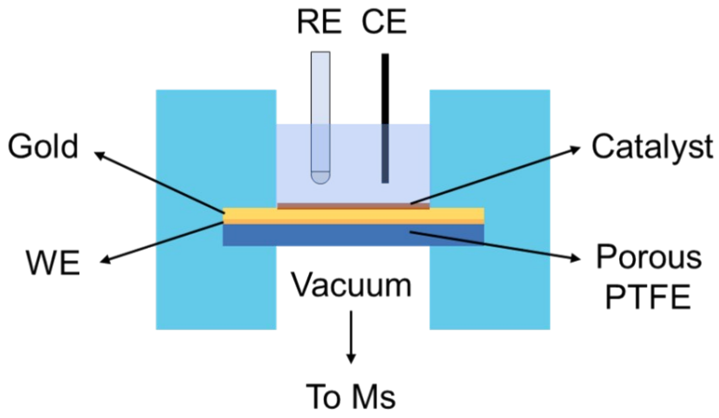

Figure S32. The schematic illustration of the DEMS technique.

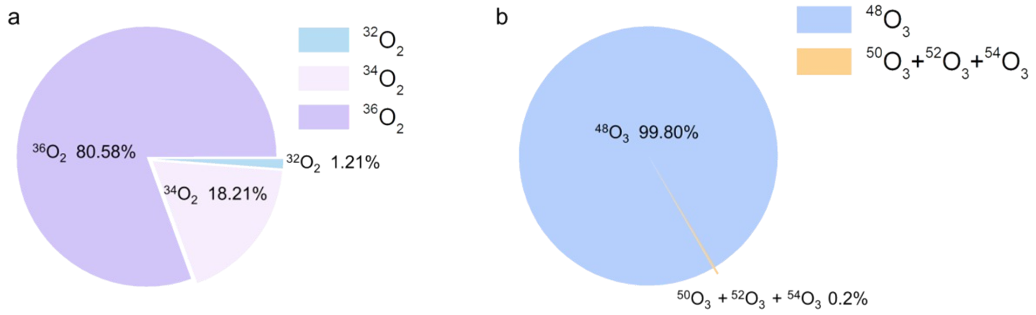

Figure S33. (a, b) O_2 and O_3 component content on Pb_3O_4 during the EOP process at 2.4V *vs.* RHE by in situ DEMS.

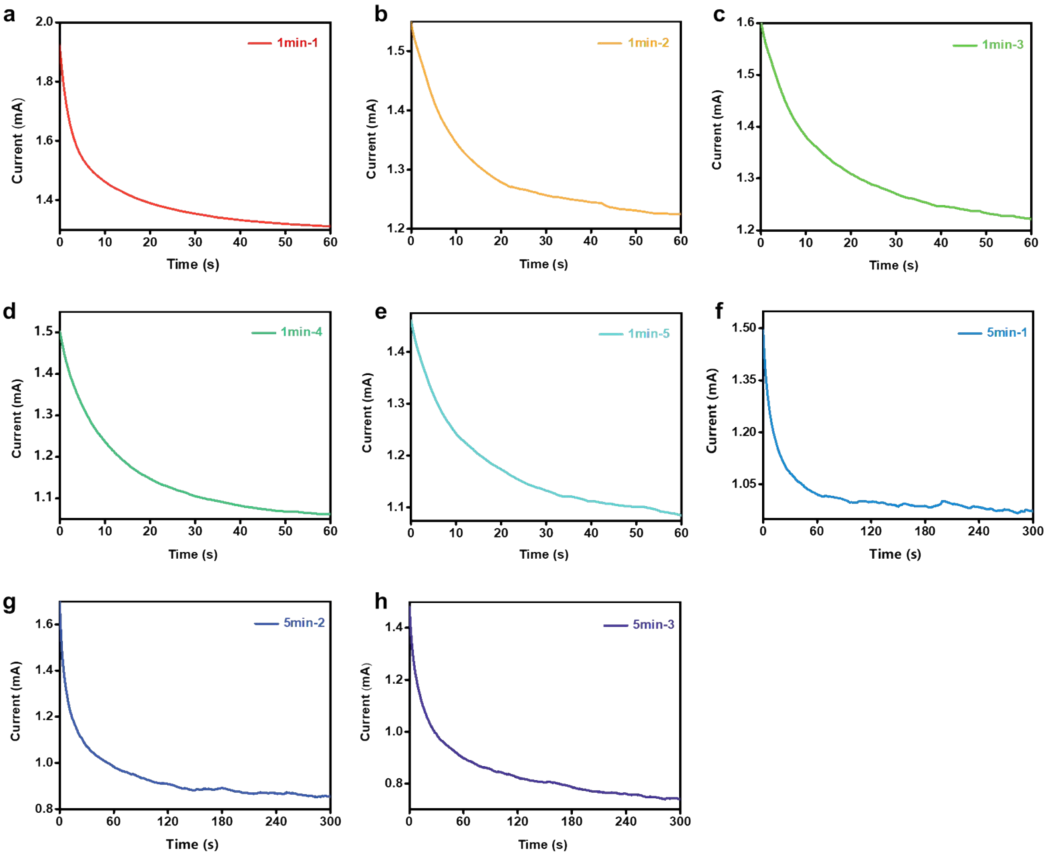

Figure S34. Kinetic current recorded in ^{18}O -enriched saturated K_2SO_4 electrolyte prepared using $H_2{}^{18}O$ on Pb_3O_4 at E (*vs.* RHE) = 2.4 V *vs.*RHE for 20min.

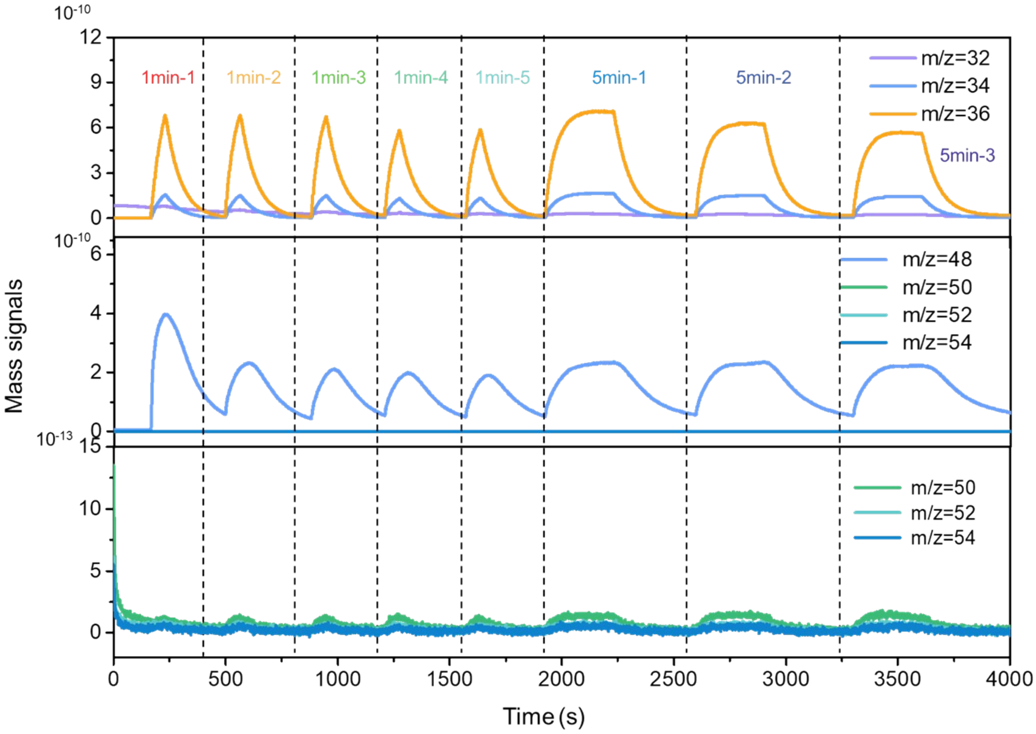

Figure S35. DEMS signals of m/z=32, m/z=34, m/z=36, m/z=48, m/z=50, m/z=52 and m/z=54 from the reaction products in saturated $K_2SO_4(H_2{}^{18}O)$ neutral electrolyte based Pb_3O_4 electrocatalysts at the same process of **Supplementary Fig. 34**.

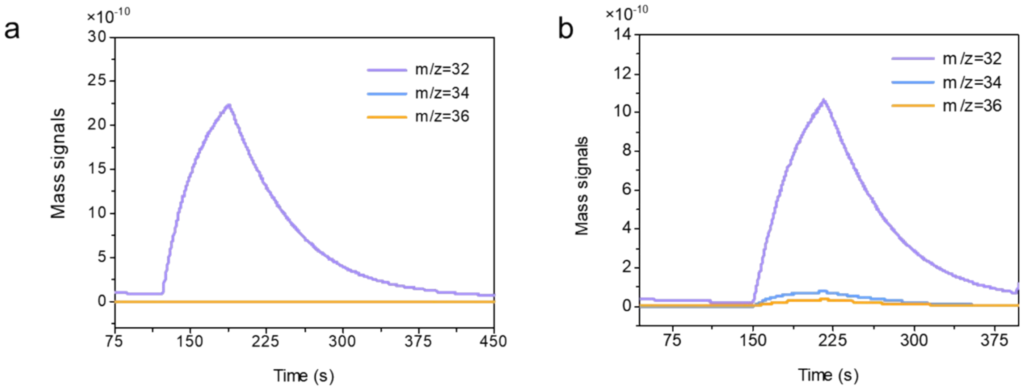

Figure S36. Direct evidence of lattice oxygen oxidation involved in the OER of ^{18}O-labelled Pb_3O_4. (a, b) DEMS signals of m/z=32, m/z=34, and m/z=36 from the reaction products in saturated $K_2SO_4(H_2{}^{16}O)$ neutral electrolyte on Pb_3O_4 electrocatalysts before and after isotope-labeled experiments by using ^{18}O-labelled at E (*vs.* RHE) = 2.4 V *vs.*RHE.

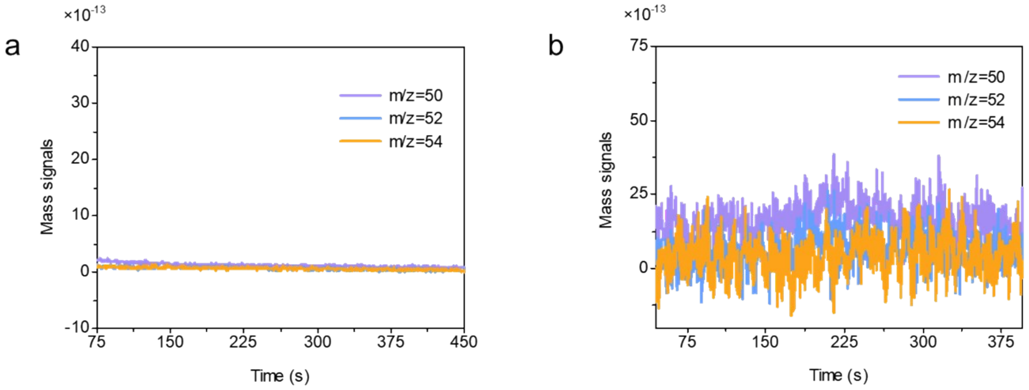

Figure S37. Direct evidence of lattice oxygen oxidation involved in the EOP of ^{18}O-labelled perovskites. a, b DEMS signals of m/z=50, m/z=52, and m/z=54 from the reaction products in saturated $K_2SO_4(H_2{}^{16}O)$ neutral electrolyte based Pb_3O_4 before and after isotope-labeled experiments by using ^{18}O-labelled at E (*vs.* RHE) = 2.4 V *vs.*RHE.

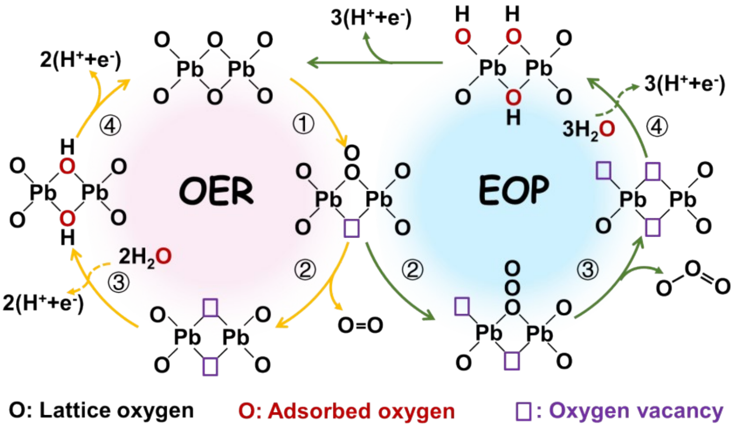

Figure S38. Proposed reaction network of O_2/O_3 formation via the lattice oxygen mechanism.

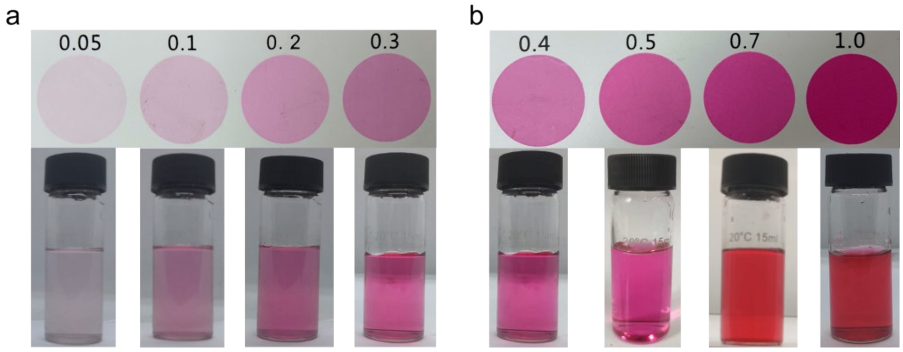

Figure S39. (a-b) Ozonated water qualitative concentration test result, in which the color depth represents the concentration of dissolved ozone (mg/L).

Method for testing: Add a packet of ozone powder reagent to 10mL of the sample water, shake well to dissolve the reagent as completely as possible, and complete the testing within one minute.

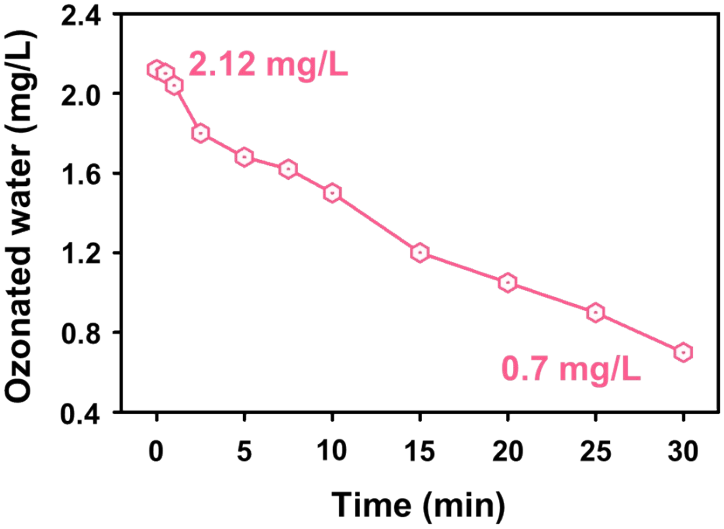

Figure S40. The curve of declining ozonated water concentration is based on Figure 5.

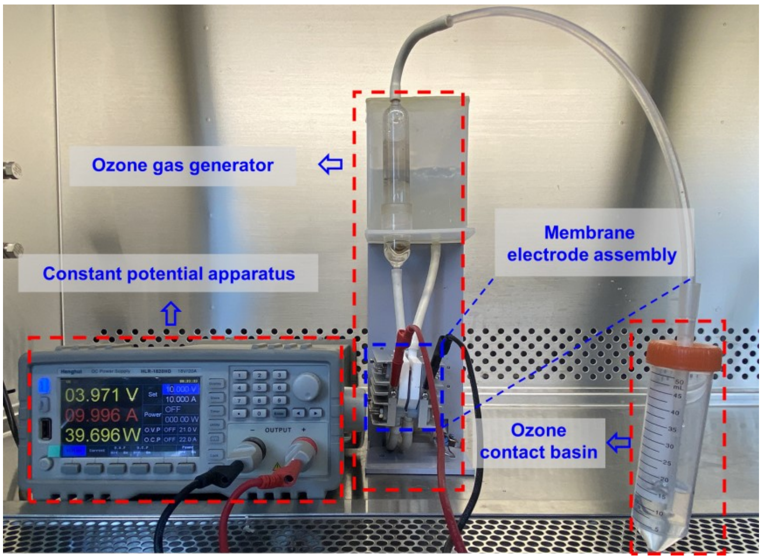

Figure S41. Real-life image of ozonated water being collected through the EOP electrolyzer.

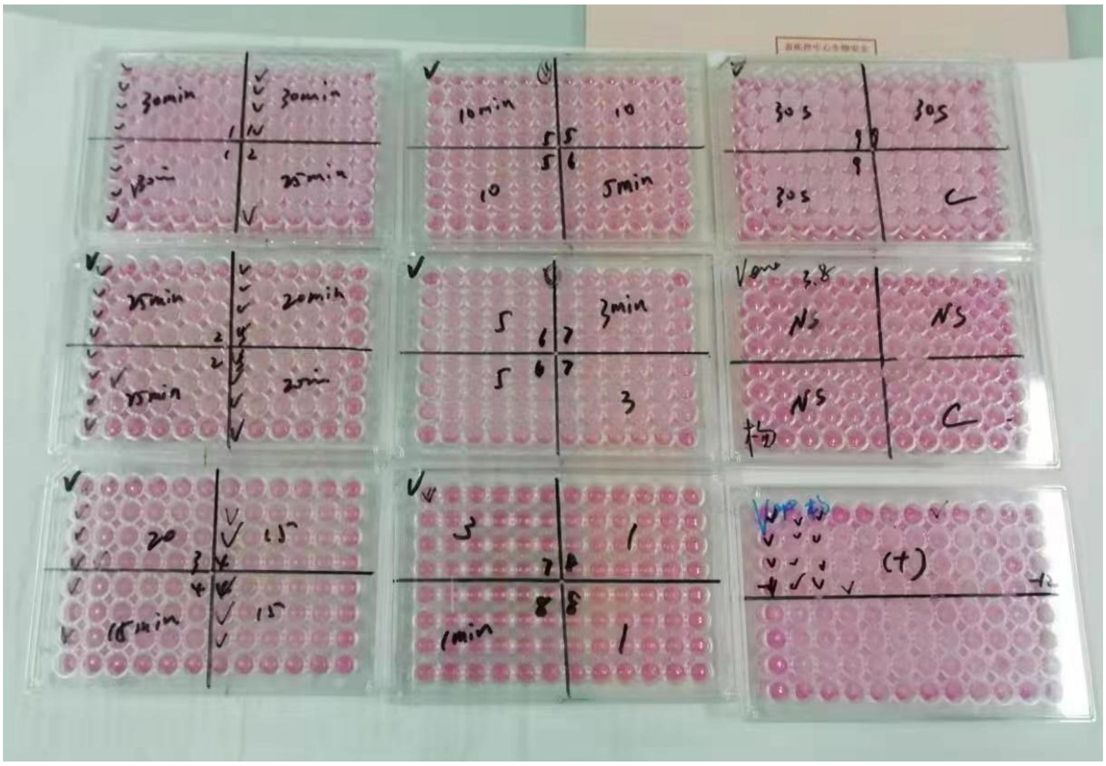

Figure S42. The photograph of the infection process of Vero cells in 96-well plates (Corresponding Fig.5a).

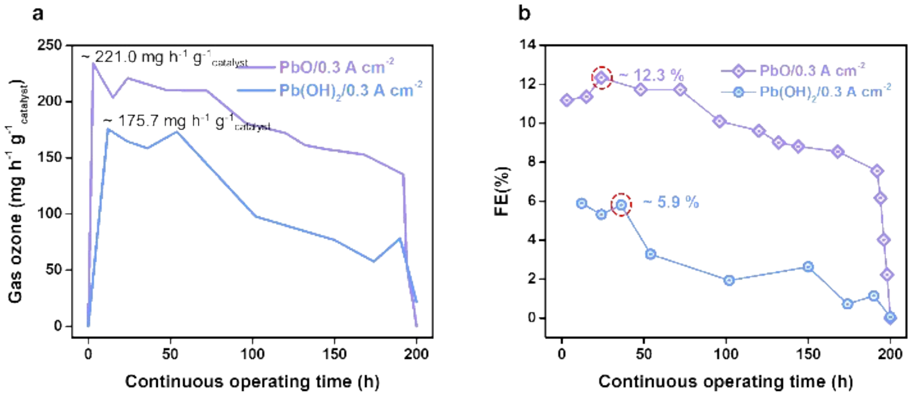

Figure S43. a, Gaseous ozone output (a) and faradaic efficiency (b) of the EOP electrolyzer with an anode of commercial PbO and $Pb(OH)_2$ for 200 h at the constant current condition of 0.3 A cm^{-2}.

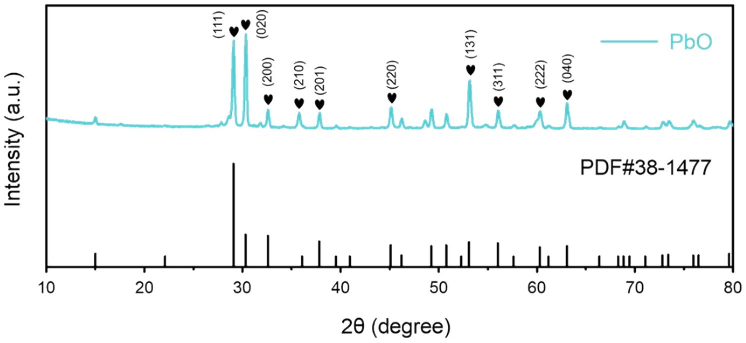

Figure S44. XRD patterns of commercial PbO and the standard patterns of PbO (PDF # 38-1477).

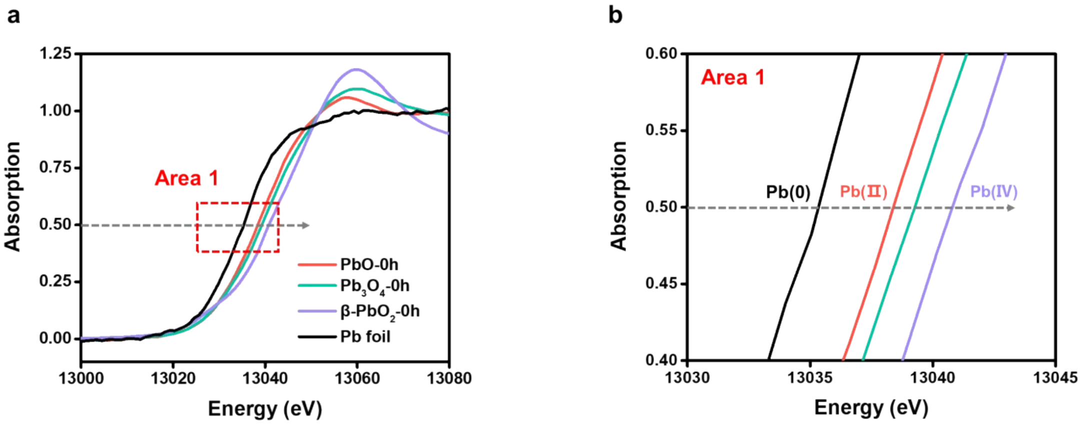

Figure S45. The XANES Pb L_3-edge spectra of Pb foil, PbO, Pb_3O_4 and β-PbO_2.

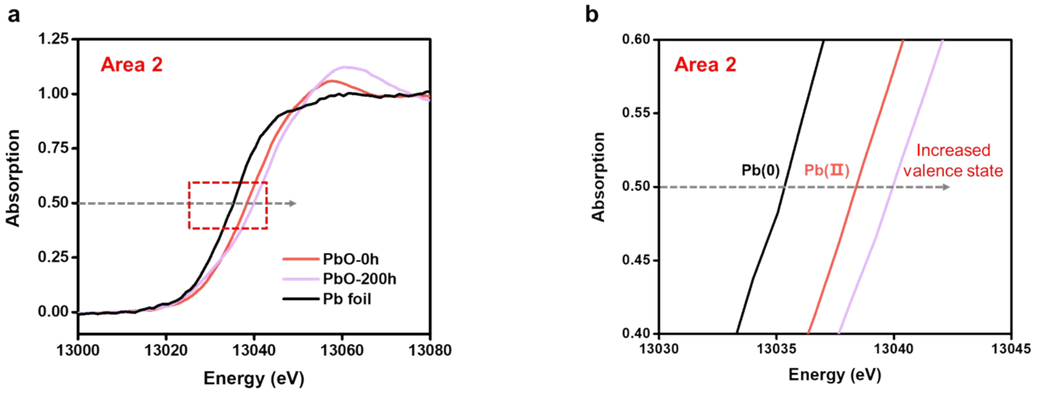

Figure S46. XAFS analysis of PbO under different EOP durations.

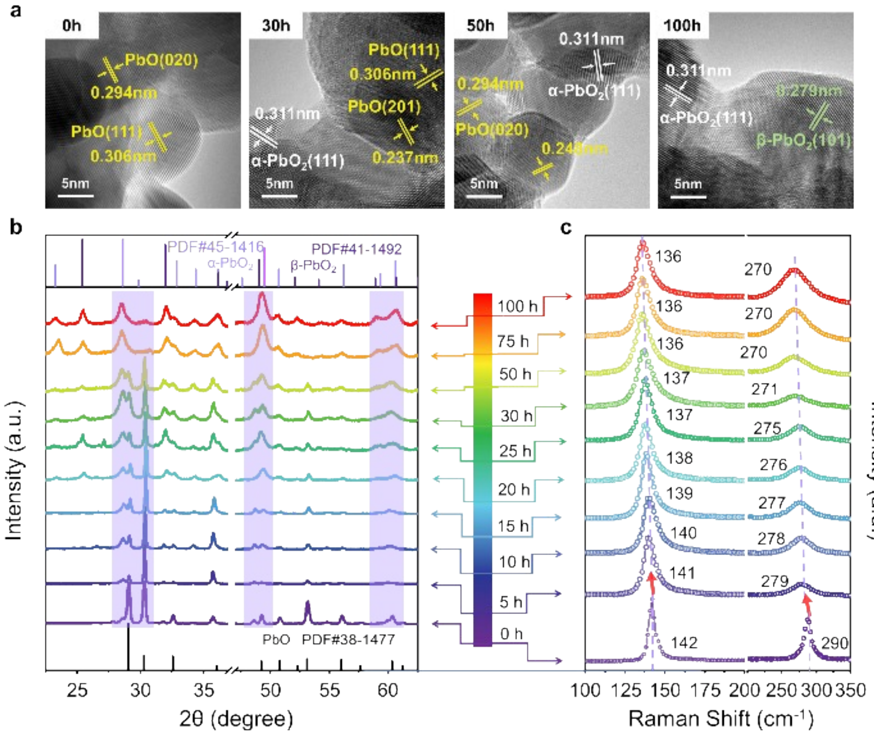

Figure S47. a, HRTEM images b, Ex situ XRD patterns, c, Ex situ Raman spectra based before and after EOP treatment in EOP electrolyzer at a current of 0.3 A cm^{-2}.

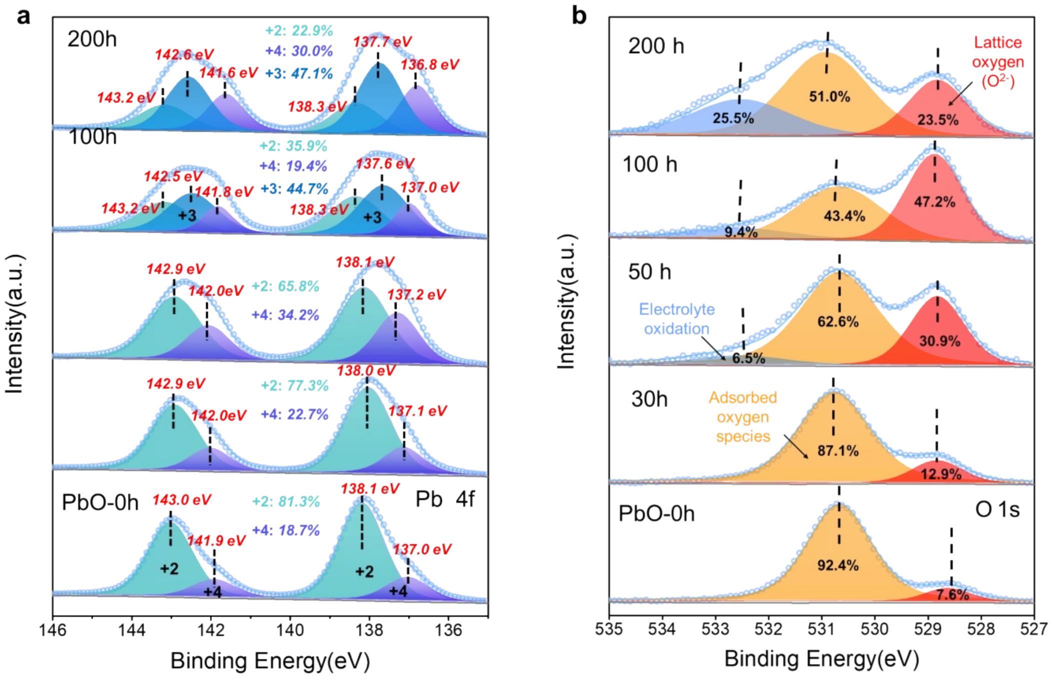

Figure S48. Pb 4f spectra, and e, O1s spectra of PbO based before and after EOP treatment in EOP electrolyzer at a high current of 0.3 A cm^{-2}.

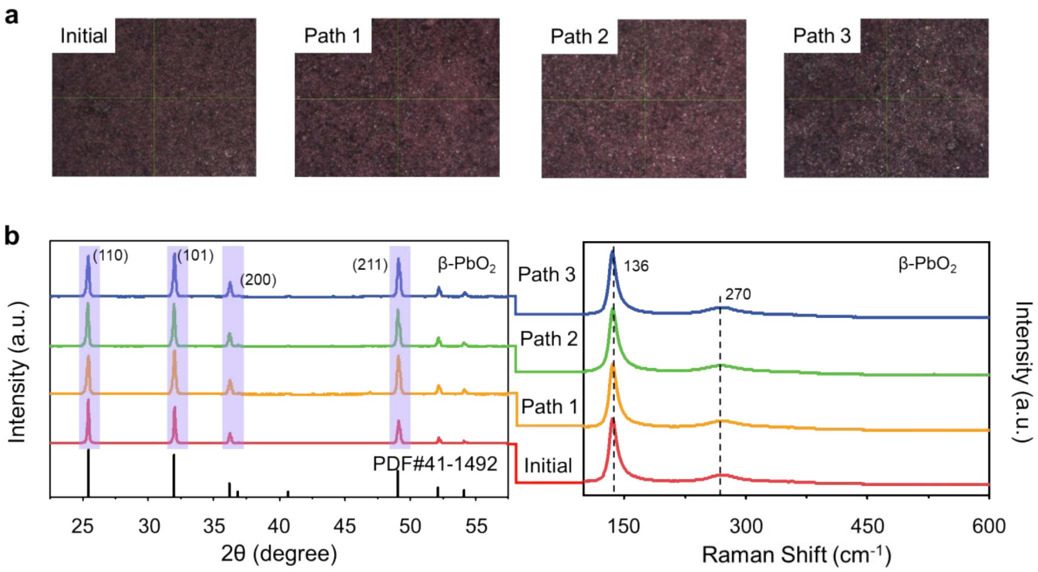

Figure S49. Potential-dependent of the Reconstruction by β-PbO$_2$. (a) 50x images, (b) Ex situ XRD patterns, and (c) Ex situ Raman spectra of β-PbO$_2$ based samples after the EOP process at various working potentials for 30h. For reaction paths 1, 2, and 3, the anode potentials are 2.4-2.45 V, 1.8-1.9 V, and 1.2-1.4 V *vs.*RHE, respectively.

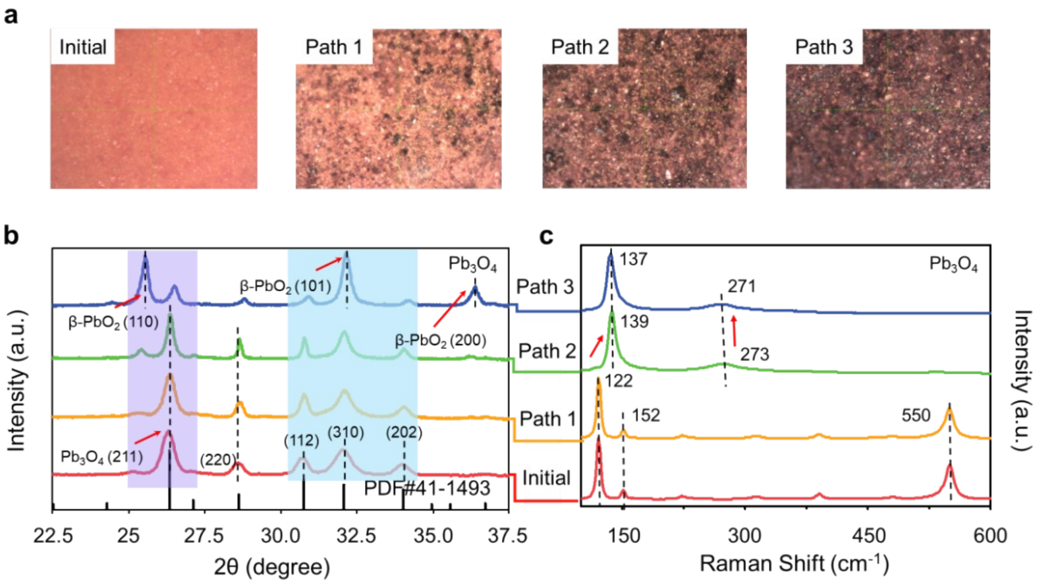

Figure S50. Potential-dependent of the Reconstruction by Pb_3O_4. (a) 50x images, (b) Ex situ XRD patterns, and (c) Ex situ Raman spectra of Pb_3O_4 after the EOP process at different working conditions for 30h. For reaction paths 1, 2, and 3, the anode potentials are 2.4-2.45 V, 1.8-1.9 V, and 1.2-1.4 V *vs.*RHE, respectively.

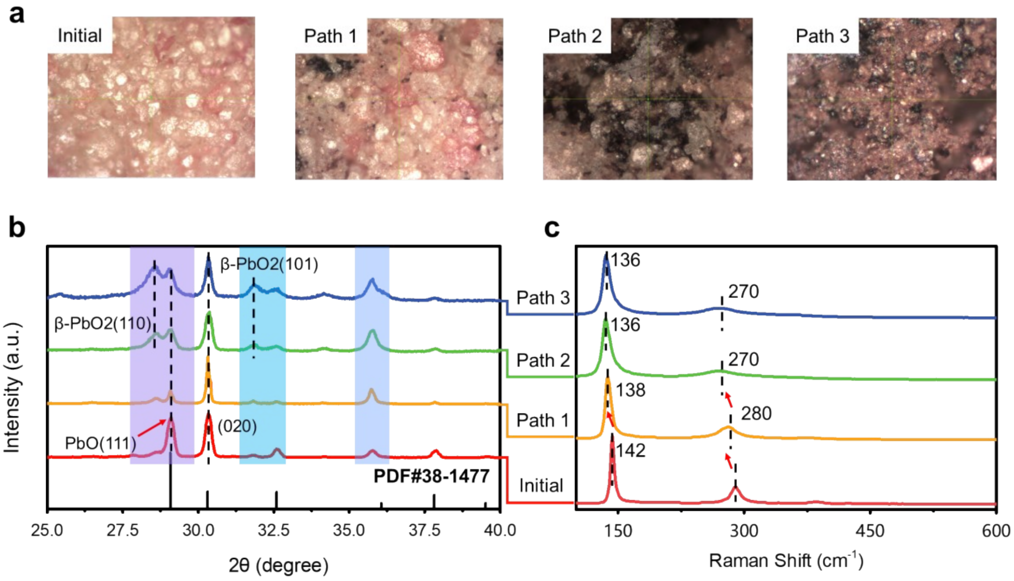

Figure S51. Potential-dependent of the Reconstruction by PbO. (a) 50x images, (b) Ex situ XRD patterns, and (c) Ex situ Raman spectra of PbO after the EOP process at different working conditions for 30h. For reaction paths 1, 2, and 3, the anode potentials are 2.4-2.45 V, 1.8-1.9 V, and 1.2-1.4 V *vs.*RHE, respectively.

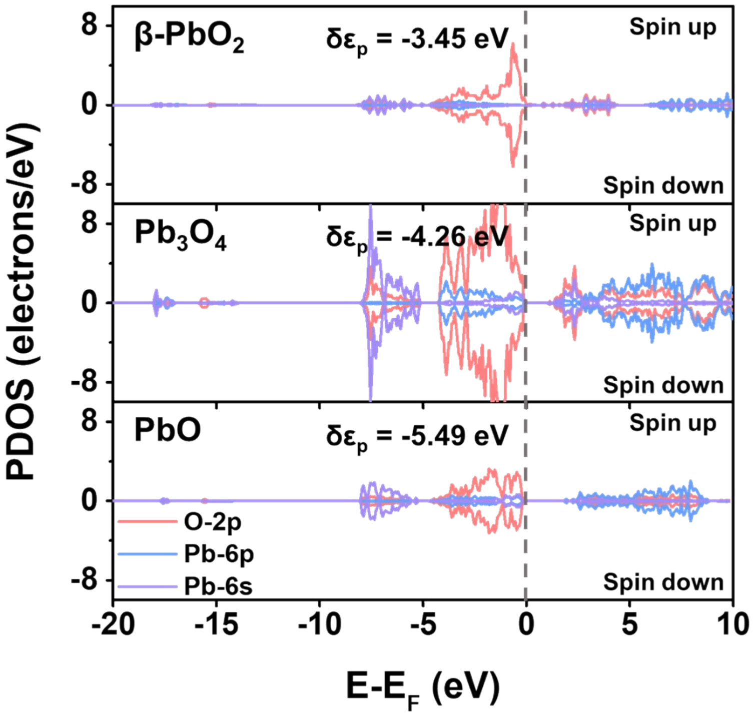

Figure S52. DFT calculated projected density of states (PDOS) for the bulk PbO, PbO_2, and Pb_3O_4 structure. Oxygen p-band centers for all lattice oxygen atoms ($\delta\varepsilon_p$) in the above bulk phases were also calculated and shown in the figure.

The projected density of states for the bulk PbO, PbO_2, and Pb_3O_4 structure were also calculated and shown in Supplementary Figure 52. The oxygen p-band center ($\delta\varepsilon_p$) with respect to the fermi level were also calculated to reveal the distribution of the oxygen valence orbital (*2p*), which can also be used to evaluate the reactivity of the lattice oxygen atoms for the above three phases[11, 12]. The $\delta\varepsilon_p$ with respect to the fermi level was calculated by the following equation:

$$\delta\varepsilon_p = \frac{\int_{-\infty}^{+\infty} E \times PDOS(E)dE}{\int_{-\infty}^{+\infty} PDOS(E)dE} - E_{fermi}$$

Note that the $\delta\varepsilon_p$ values calculated in this work could only give the qualitative descriptions for the reactivity of the lattice oxygen atoms in the bulk phase, since the lattice oxygen atoms are likely to have different coordinating conditions and the PDOS referred to all the lattice oxygens. Thus, the $\delta\varepsilon_p$ values were averaged when evaluating different oxygen sites. The $\delta\varepsilon_p$ value for the PbO_2 was calculated to be -3.45 eV, which was more close to the Fermi level in contrast to the PbO and Pb_3O_4, indicating the higher reactivity of the lattice oxygen in the PbO_2 phase, which also accounts for the superior reactivity of the PbO_2 phase in experiment. By comparing the three phases, it is possible to conclude that the reactivity of lattice oxygen atoms follows the order of $PbO_2 > Pb_3O_4 > PbO$.

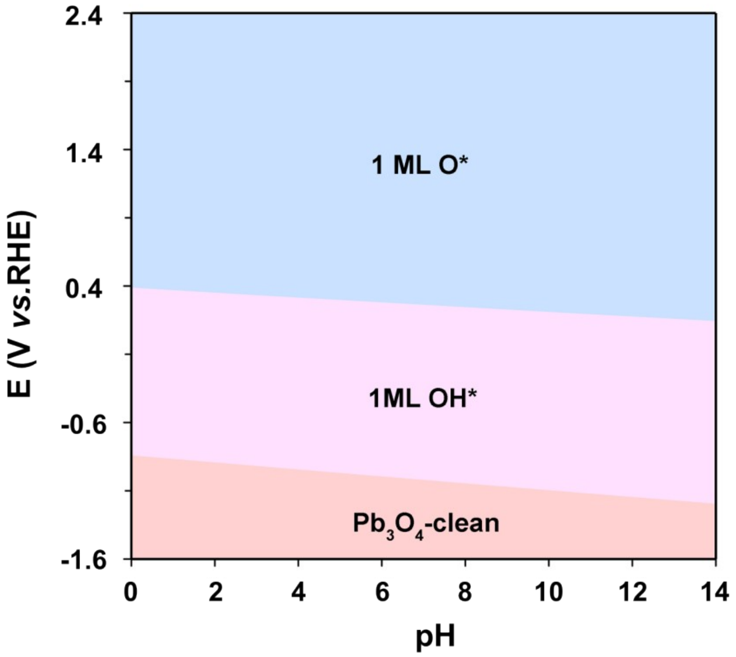

Figure S53. DFT calculated pH-potential phase diagram of the β-Pb_3O_4(110) surface. The phase diagram is constructed for the lead oxide surfaces with total OH*/O* occupation.

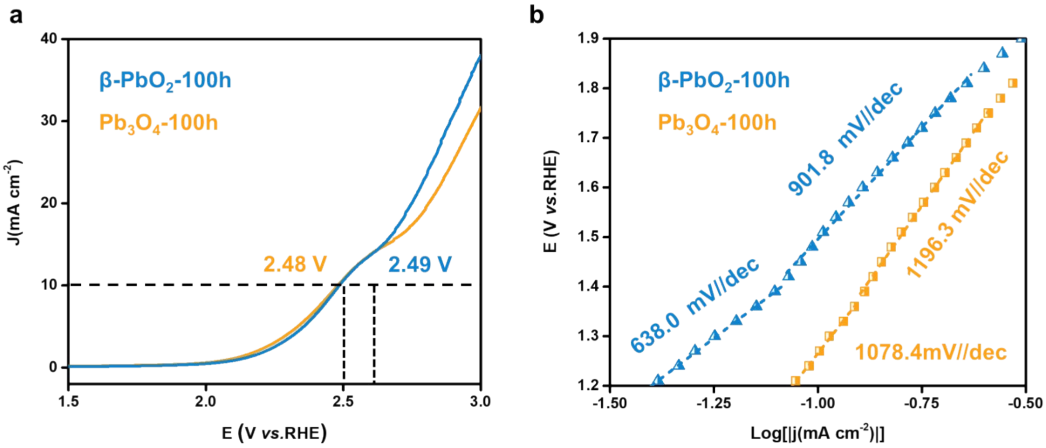

Figure S54. Steady-state polarization curves and corresponding Tafel slopes of commercial β-PbO_2 and Pb_3O_4 in saturated K_2SO_4 solution after 100 h EOP test. (pH = 7.0).

As shown from steady-state polarization curves in Supplementary Figure 1a, a potential of 2.48 V vs. RHE was required for the Pb_3O_4-100h sample to achieve the current density of 10 mA cm^{-2}, which is about the same as β-PbO_2-100h sample (2.49 V vs. RHE). Tafel slopes of β-PbO_2-100 h sample and Pb_3O_4-100 h sample delivered 638 mV/dec and 1078.4 mV/dec, respectively at a low current density region. Tafel slopes for both electrocatalysts were observable at high current density/applied potential, where Tafel slopes of β-PbO_2-100 h sample and Pb_3O_4-100 h sample were 901.8 mV/dec and 1196.3 mV/dec, respectively. These results indicated that β-PbO_2-100 h sample exhibited more favorable reaction kinetics than Pb_3O_4-100h sample in the anodic reaction process thus provided better EOP reaction performance.

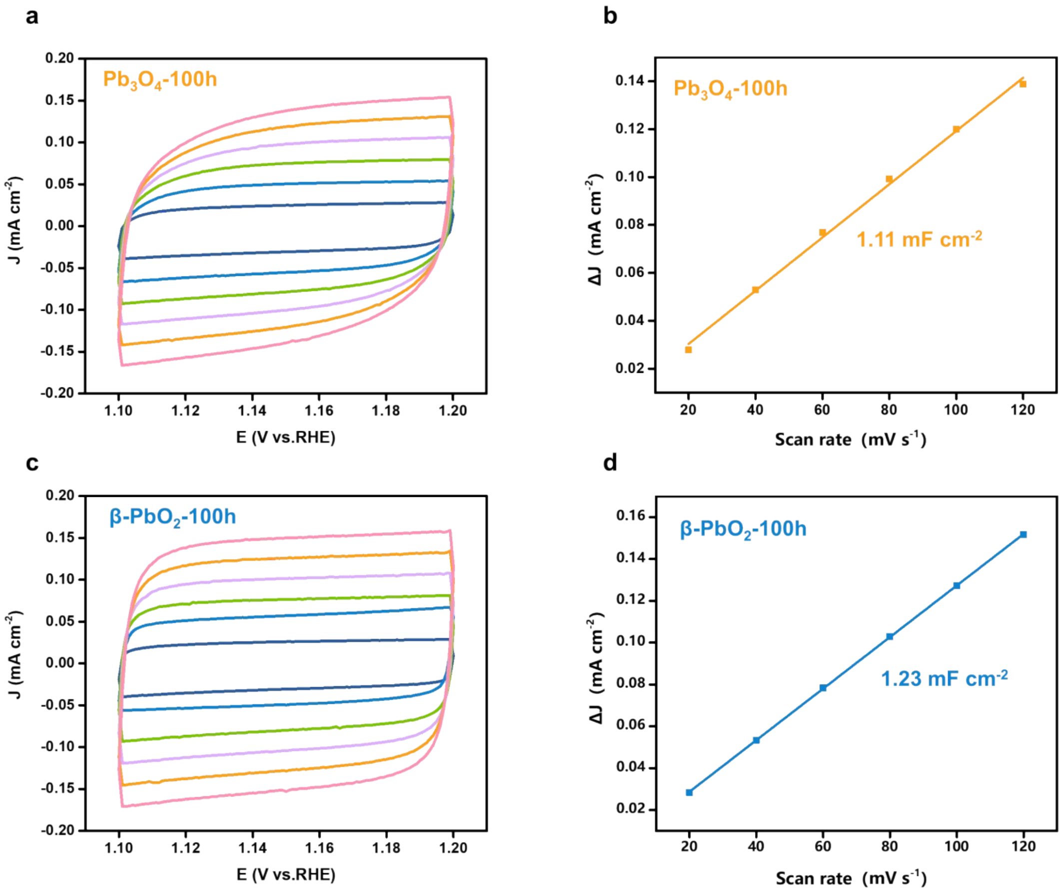

Figure S55. Cyclic voltammetry curves at various scan rates of 20, 40, 60, 80, 100, and 120 mV s^{-1} in saturated K_2SO_4 solution of Pb_3O_4-100 h sample (a) and β-PbO_2-100 h sample (c) for the determination of double-layer capacitance. Different scan rates to measure capacitive currents for Pb_3O_4-100 h sample (b) and β-PbO_2-100 h sample (d).

To assess the intrinsic EOP activity of the electrocatalysts, electrochemical two-layer capacitance (C_{dl}) was measured to determine the electrochemical active surface area (ECSA). In Supplementary Figure XXX, it could be seen that Pb_3O_4-100 h sample (1.11 mF cm^{-2}) and β-PbO_2-100 h sample (1.23 mF cm^{-2}) had similar C_{dl} values, suggesting that their effective active surface areas were almost the same. These results suggested that β-PbO_2-100h sample presented better EOP reaction performance mainly due to its high intrinsic activity.

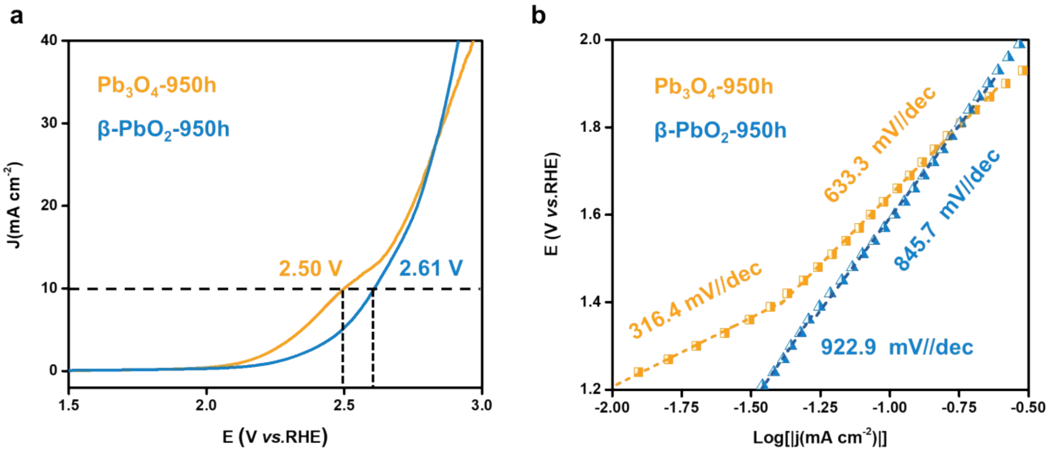

Figure S56. Steady-state polarization curves and corresponding Tafel slopes of commercial β-PbO_2 and Pb_3O_4 in saturated K_2SO_4 solution after 950 h EOP test. (pH = 7.0).

As shown from steady-state polarization curves in Supplementary Figure 1a, a potential of 2.50 V vs. RHE was required for the Pb_3O_4-950h sample to achieve the current density of 10 mA cm^{-2}, which was lower than β-PbO_2-950h sample (2.61 V vs. RHE). Tafel slopes of β-PbO_2-950 h sample and Pb_3O_4-950 h sample delivered 922.9 mV/dec and 316 mV/dec, respectively at a low current density region. Tafel slopes for both electrocatalysts were observable at high current density, where Tafel slopes of β-PbO_2-950 h sample and Pb_3O_4-950 h sample were 845.7 mV/dec and 633.3 mV/dec, respectively. These results indicated that Pb_3O_4-950 h sample exhibited more favorable reaction kinetics than β-PbO_2-950 h sample in the anodic reaction process thus provided better EOP reaction performance.

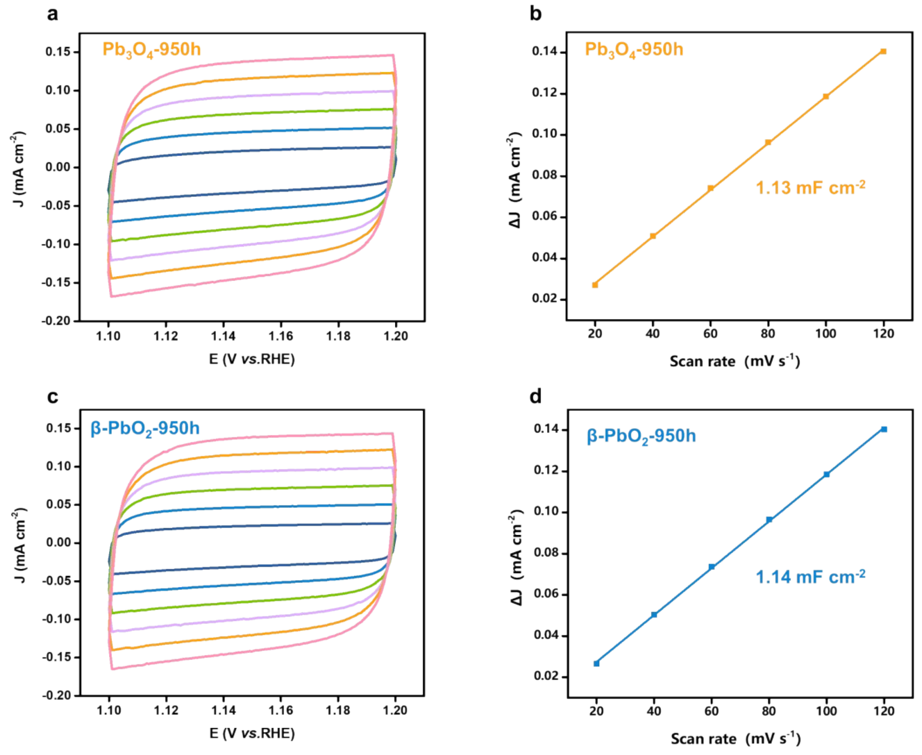

Figure S57. Cyclic voltammetry curves at various scan rates of 20, 40, 60, 80, 100, and 120 mV s^{-1} in saturated K_2SO_4 solution of Pb_3O_4-950 h sample (a) and β-PbO_2-950 h sample (c) for the determination of double-layer capacitance. Different scan rates to measure capacitive currents for Pb_3O_4-950 h sample (b) and β-PbO_2-950 h sample (d).

To assess the intrinsic EOP activity of the electrocatalysts, electrochemical two-layer capacitance (C_{dl}) was measured to determine the electrochemical active surface area (ECSA). In Supplementary Figure 56, it could be seen that Pb_3O_4-950 h sample (1.13 mF cm^{-2}) and β-PbO_2-950 h sample (1.14 mF cm^{-2}) had similar C_{dl} values, suggesting that their effective active surface areas were almost the same. These results suggested that Pb_3O_4-950 h sample presented better EOP reaction performance mainly due to its high intrinsic activity.

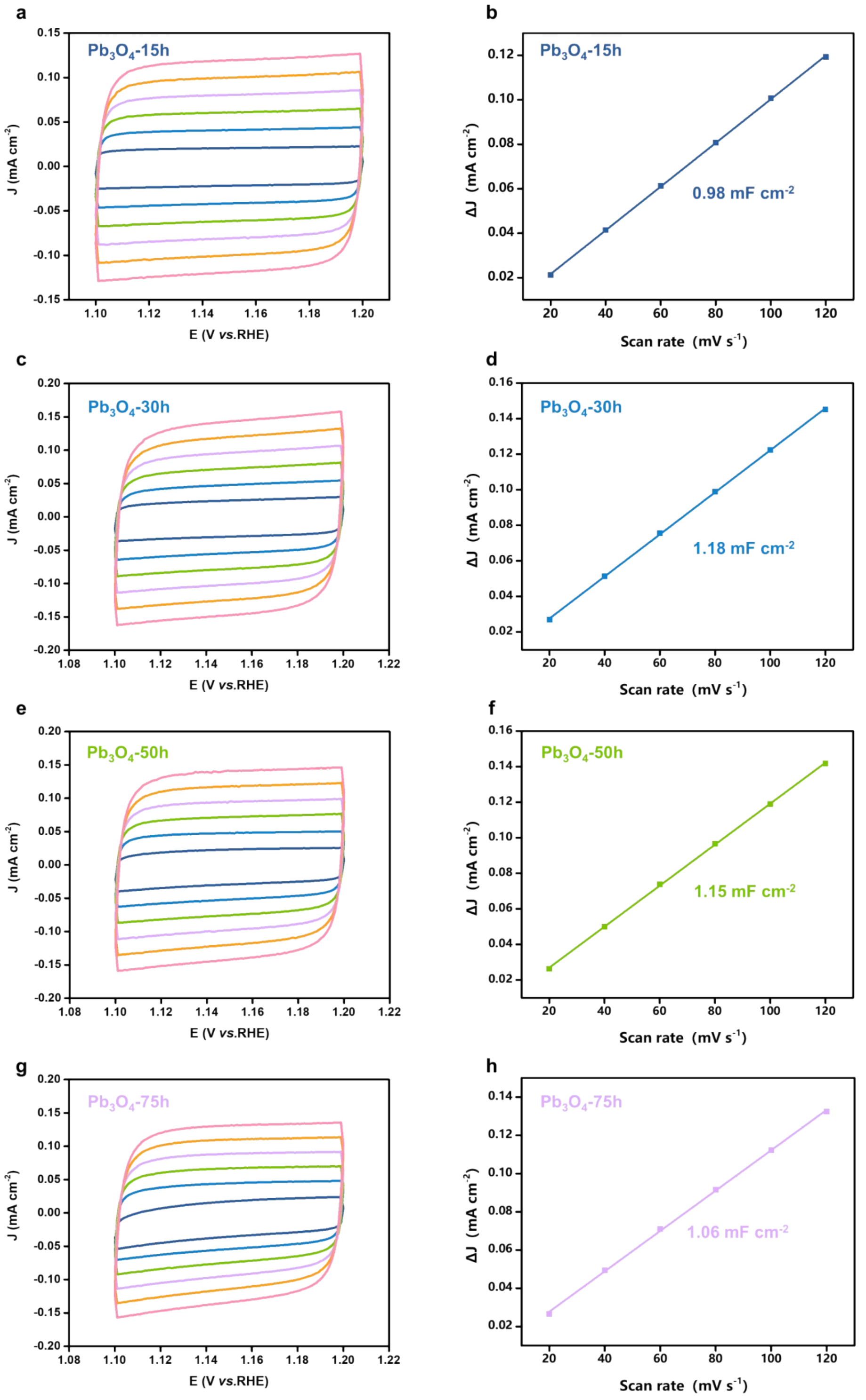

Figure S58. a, c, e, and g, cyclic voltammetry curves at various scan rates of 20, 40, 60, 80, 100, and 120 mV s^{-1} in saturated K_2SO_4 solution of Pb_3O_4 for the determination of double-layer capacitance under different EOP duration. b, d, f and h, different scan rates to measure capacitive currents for Pb_3O_4 under different EOP duration.

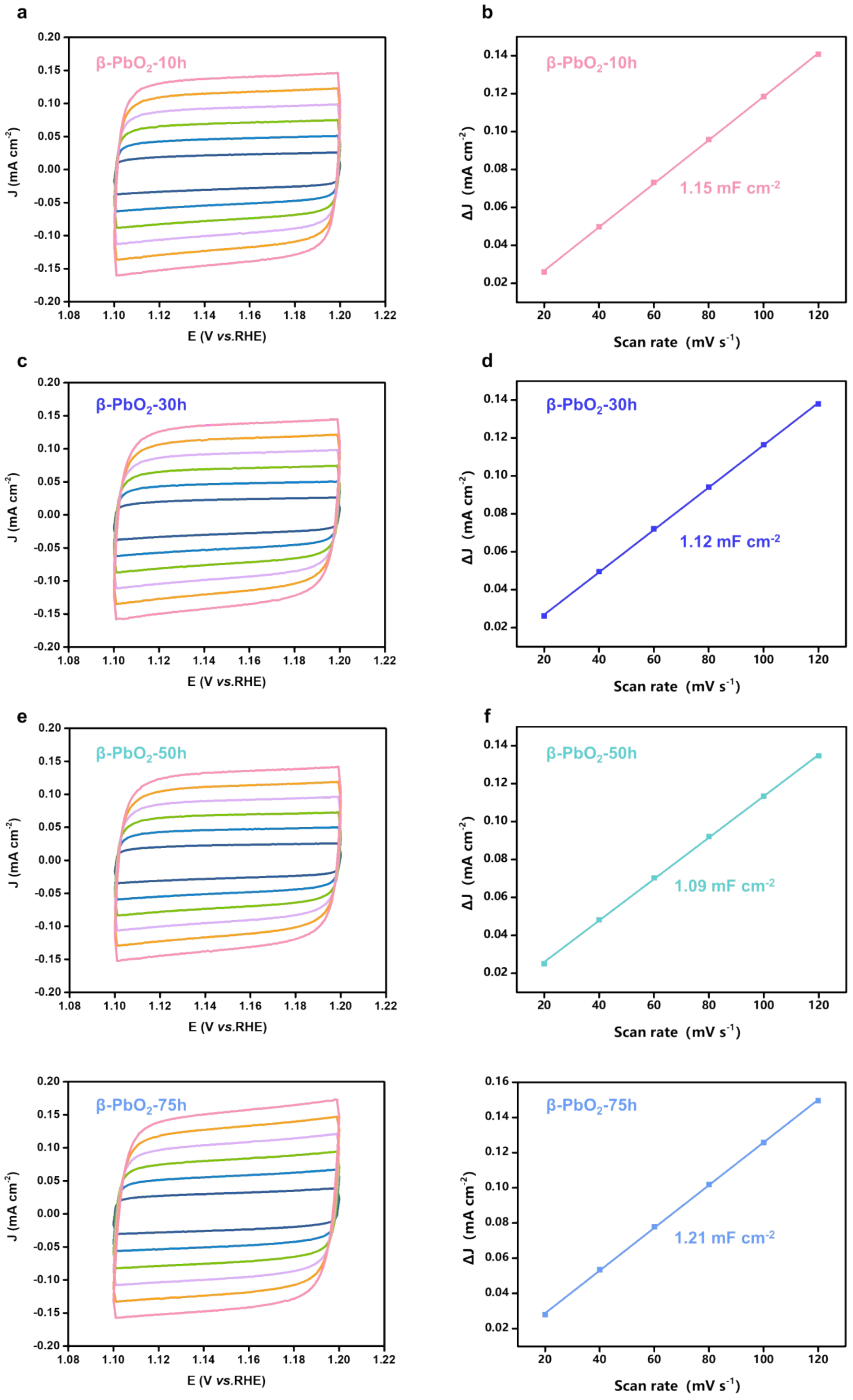

Figure S59. a, c, e, and g, cyclic voltammetry curves at various scan rates of 20, 40, 60, 80, 100, and 120 mV s^{-1} in saturated K_2SO_4 solution of β-PbO_2 for the determination of double-layer capacitance under different EOP duration. b, d, f and h, different scan rates to measure capacitive currents for β-PbO_2 under different EOP duration.

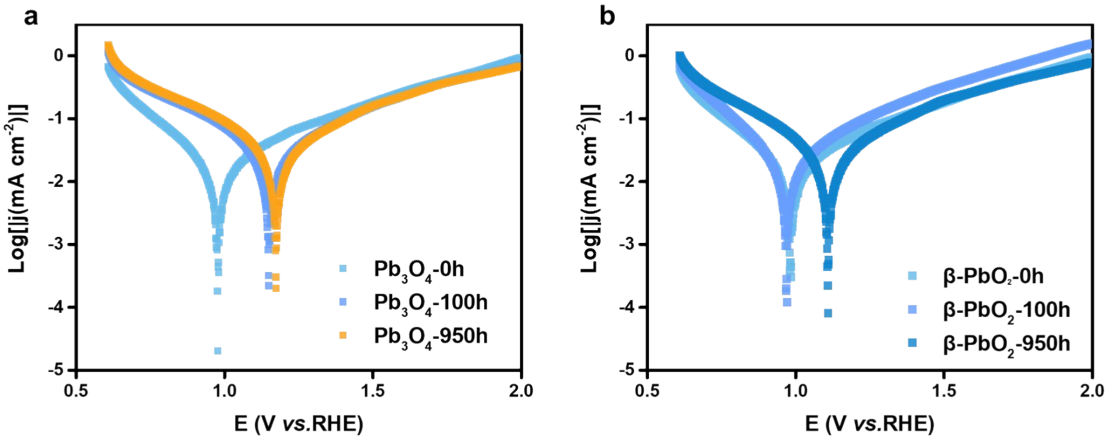

Figure S60. Corrosion polarization curves of Pb_3O_4 and β-PbO_2 under different EOP duration.

The corrosion polarization curves of Pb_3O_4-100 h sample and Pb_3O_4-950 h sample almost overlapped, which indicates that the Pb_3O_4 precatalyst could maintain good stability during the EOP operation. In addition, the corrosion polarization curves of β-PbO_2-100h sample and β-PbO_2-950h sample were different, which indicates that the stability of this material changed a lot during the EOP operation.

Table S1. The Tafel slope comparison of Pb_3O_4 with other electrocatalysts toward EOP.

Catalysts	**Electrolyte**	**Temperature**	**Tafel slope at low current density region (mV dec^{-1})**	**Tafel slope at high current density region (mV dec^{-1})**	**References**
β-PbO_2/Ta_2O_5 NRs	Neutral media	25 °C	184	821	*Ref* [9, 13]
PtZn/Zn-N-C	Neutral media	25 °C	798.9	749.1	*Ref* [14]
D-BNC	Neutral media	25 °C	663	977	*Ref* [15]
β-PbO_2-120	Neutral media	25 °C	737.5	1791.8	*Ref* [16]
Pt-SAs/BNC-3	Neutral media	25 °C	367	994	*Ref* [17]
$Bi_{12}PbO_{20}$-3	Neutral media	25 °C	306	667	*Ref* [18]
Pb_3O_4	Neutral media	25 °C	434	681	This work

Table S2. The performance comparison of Pb_3O_4 with other electrocatalysts toward EOP.

Catalysts	Electrolyte	Temperature	FE (%)	J (mA/cm^{-2})， Stability test	References
n-Type TiO_2	Acid medium	15 °C	9	8.9 mA/cm^2, /	*Ref*[19]
Si/TiO_x/Pt/TaO_x	Acid medium	25 °C	1.3	30 mA/cm^2,/	*Ref*[20]
Pt-TaO_y	Neutral media	25 °C	19.3	100 mA/cm^2, /	*Ref*[21]
D-BNC	Neutral media	25 °C	1.7	20mA/cm^2, 100 h	*Ref*[15]
PtZn/Zn-N-C	Neutral media	25 °C	4.2	3 V *vs.*RHE (~10mA/cm^2), 20 h	*Ref*[14]
Pt-Loaded Reticulated Vitreous Carbon(RVC/Pt)	Acid medium	25 °C	2.2	80 mA/cm^2, 20h	*Ref*[22]
Pt-TaO_x/Ti	Neutral media	25 °C	11.7	~50 mA/cm^2, 60 h	*Ref*[23]
β-PbO_2-120	Ultrapure water	25 °C	14.9	0.5 A/cm^2, 50 h	*Ref*[16]
β-PbO_2/Ta_2O_5 NRs	Neutral media	25 °C	16.4	3 V *vs.*RHE (~10mA/cm^2), 100 h	*Ref*[13]
Pt-SAs/BNC-3	Neutral media	25 °C	21	3 V *vs.*RHE (~10mA/cm^2), 100 h	*Ref*[17]
$Bi_{12}PbO_{20}$-3	Neutral media	25 °C	15.1	2.8 V *vs.*RHE (~10 mA/cm^2) ,100 h	*Ref*[18]
Pb_3O_4	**Ultrapure water**	**25 °C**	**~12**	**1 A/cm^2, 500 h**	**This work**

Table S3. The relative concentration of different O species based on XPS of the Pb_3O_4 under different EOP durations.

Samples	The relative concentration of different O species (area %)		
	Electrolyte oxidation	Adsorbed oxygen species	Lattice oxygen
Pb_3O_4-0 h	0	41.2	58.8
Pb_3O_4-15 h	4.8	38.1	57.1
Pb_3O_4-30 h	4.1	41.1	54.5
Pb_3O_4-50 h	2.7	45.3	52.0
Pb_3O_4-100 h	4.6	46.6	48.8
Pb_3O_4-500 h	5.8	47.1	47.1
Pb_3O_4-950 h	9.3	49.1	41.6

Table S4. The relative concentration of different O species based on XPS of the β-PbO_2 under different EOP durations.

Samples	**The relative concentration of different O species (area %)**		
	Electrolyte oxidation	**Adsorbed oxygen species**	**Lattice oxygen**
β-PbO_2-0 h	0	27.2	64.5
β-PbO_2-100 h	7.4	41.2	51.4
β-PbO_2-500 h	13.3	41.0	45.7
β-PbO_2-950 h	8.8	54.9	36.3

Table S5. The relative concentration of different Pb species based on XPS of the Pb_3O_4 under different EOP durations[25, 26].

Samples	**The relative concentration of different Pb species (area %)**		
	Pb^{2+}	**Pb^{4+}**	**Pb^{3+}**
Pb_3O_4-0 h	/	/	/
Pb_3O_4-15 h	/	/	/
Pb_3O_4-30 h	23.5	36.3	40.2
Pb_3O_4-50 h	27.9	15.8	56.3
Pb_3O_4-100 h	25.6	33.6	40.8
Pb_3O_4-500 h	20.0	36.2	43.8
Pb_3O_4-950 h	20.0	41.9	38.1

Table S6. The relative concentration of different Pb species based on XPS of the β-PbO_2 under different EOP durations[27, 28].

Samples	**The relative concentration of different Pb species (area %)**		
	Pb^{2+}	**Pb^{4+}**	**Pb^{3+}**
β-PbO_2-0 h	/	/	/
β-PbO_2-100 h	25.6	33.6	40.8
β-PbO_2-500 h	20.0	36.2	43.8
β-PbO_2-950 h	20.0	41.9	38.1

Table S7. The valence of Pb element obtained from the curve-fitting analysis of the EXAFS spectrum.

Samples	**Valence**
Pb power	0
PbO-0 h	2.07
PbO-200 h	3.13
Pb_3O_4-0 h	2.67
Pb_3O_4-500 h	3.15
Pb_3O_4-950 h	3.77
β-PbO_2-0 h	4.00
β-PbO_2-500 h	3.94
β-PbO_2-950 h	3.75

Table S8. Structural parameters obtained from the curve-fitting analysis of the EXAFS spectrum (First shell fitting with Feff [a]).

Samples	Path	Reff (Å) [b]	R (Å)	CN [c]	ΔE_0 (eV) [d]	σ^2 (Å^2) [e]	R factor
Pb_3O_4-0 h	Pb-O1	2.181	2.147 (±0.011)[f]	1.3 (±0.2)	-2.5 (±1.3)	0.003(±0.002) [g]	1.2%
	Pb-O2	2.249	2.214 (±0.012)[f]	2.7 (±0.3)			
Pb_3O_4-500 h	Pb-O	2.206	2.157 (±0.011)	4.1 (±0.5)	-2.3 (±1.3)	0.003 (±0.002)	1.0%
Pb_3O_4-950 h	Pb-O	2.206	2.156 (±0.013)	4.3 (±0.6)	-9.1 (±1.6)	0.003 (±0.002)	1.2%
β-PbO_2-0 h	Pb-O	2.206	2.158 (±0.016)	6.0 (±1.2)	-12.5 (±2.2)	0.003 (±0.002)	2.2%
β-PbO_2-500 h	Pb-O	2.206	2.163 (±0.014)	5.9 (±1.0)	-13.4 (±1.0)	0.002 (±0.002)	1.5%
β-PbO_2-950 h	Pb-O	2.206	2.171 (±0.011)	5.0 (±0.7)	-8.1 (±1.5)	0.001 (±0.001)	1.2%

Note: a. Data range: $2.5 \leq k1 \leq 11$, $1.2 \leq R \leq 2.5$ Å. The number of variable parameters is 4, out of 6.8 independent data points; b. The distances in FEFF files for Pb-O1 and Pb-O2 in Pb_3O_4 and Pb-O in β-PbO_2; c. Coordination number (N * S0^2); d. Energy shift; e. The mean square displace about the half path length of the path; f. Only the volumetric expansion was considered for the Pb-O1 and Pb-O2 paths in the original crystal data for decreasing the number of variables (set the ΔR = alpha * Reff for both paths); f. The Debye-Waller factors were constrained as σ^2(Pb-O1) = σ^2(Pb-O2) for reducing the number of variables.

Table S9. Mass spectroscopy peak intensity of Pb_3O_4 cycled in saturated K_2SO_4 (^{18}O labeled) to explore EOP Mechanisms.

m/z signal	**Peak intensity ($\times10^{-10}$ a.u.)**	**Intensity ratio (%)**	**Content (%) O_2 or O_3**
$^{32}O_2$	0.100	0.996	82.626
$^{34}O_2$	1.500	15.050	
$^{36}O_2$	6.680	66.580	
$^{48}O_3$	1.740	17.340	17.374
$^{50}O_3 + {}^{52}O_3 + {}^{54}O_3$	0.002	0.034	

References

1. J. Dubrail, F. Farges, L. Gautron, M. Harfouche, C. Borca and D. Grolimund, *J Phys Conf Ser*, 2009, **190**.
2. B. Saini-Eidukat, F. Melcher, J. Göttlicher and R. Steininger, *Minerals*, 2016, **6**.
3. G. Kresse and J. Furthmüller, *Comput. Mater. Sci.*, 1996, **6**, 15-50.
4. G. Kresse and J. Furthmüller, *Physical Review B*, 1996, **54**, 11169-11186.
5. J. P. Perdew, K. Burke and M. Ernzerhof, *Phys. Rev. Lett.*, 1996, **77**, 3865-3868.
6. P. E. Blöchl, *Phys. Rev. B*, 1994, **50**, 17953-17979.
7. G. Kresse and D. Joubert, *Phys. Rev. B*, 1999, **59**, 1758-1775.
8. K. Mathew, R. Sundararaman, K. Letchworth-Weaver, T. A. Arias and R. G. Hennig, *J. Chem. Phys.*, 2014, **140**, 084106.
9. W. Li, G. Feng, S. Wang, J. Liu, X. Zhong, Z. Yao, S. Deng and J. Wang, *The J. Phys. Chem. C*, 2022, **126**, 8627-8636.
10. N. J. O'Connor, A. S. M. Jonayat, M. J. Janik and T. P. Senftle, *Nat. Catal*, 2018, **1**, 531-539.
11. R. Jacobs, J. Hwang, Y. Shao-Horn and D. Morgan, *Chem. Mater.*, 2019, **31**, 785-797.
12. Z. Liu, Y. Sun, X. Wu, C. Hou, Z. Geng, J. Wu, K. Huang, L. Gao and S. Feng, *CrystEngComm*, 2019, **21**, 1534-1538.
13. Y. Yan, Y. Gao, H. Zheng, B. Yuan, Q. Zhang, Y. Gu, G. Zhuang, Z. Wei, Z. Yao and X. Zhong, *Appl. Catal. B.*, 2020, **266**, 118632.
14. B. Yuan, Z. Yao, C. Qiu, H. Zheng, Y. Yan, Q. Zhang, X. Sun, Y. Gu, X. Zhong and J. Wang, *J. Energy Chem.*, 2020, **51**, 312-322.
15. Q. Zhang, Y. Cao, Y. Yan, B. Yuan, H. Zheng, Y. Gu, X. Zhong and J. Wang, *J. Mater. Chem. A.*, 2020, **8**, 2336-2342.
16. W. Jiang, S. Wang, J. Liu, H. Zheng, Y. Gu, W. Li, H. Shi, S. Li, X. Zhong and J. Wang, *J. Mater. Chem. A.*, 2021, **9**, 9010-9017.
17. Y. Gu, S. Wang, H. Shi, J. Yang, S. Li, H. Zheng, W. Jiang, J. Liu, X. Zhong and J. Wang, *ACS Catalysis*, 2021, **11**, 5438-5451.
18. H. Shi, G. Feng, S. Li, J. Liu, X. Yang, Y. Li, Y. Lu, X. Zhong, S. Wang and J.-g. Wang, J. Mater. Chem. A., 2022.
19. K. Kitsuka, K. Kaneda, M. Ikematsu, M. Iseki, K. Mushiake and T. Ohsaka, *J. Electrochem. Soc.*, 2009, **157**, F30.
20. K. Kitsuka, K. Kaneda, M. Ikematsu, M. Iseki, K. Mushiake, A. M. Mohammad and T. Ohsaka, *Chem. Lett.*, 2007, **36**, 806-807.
21. M. I. Awad, S. Sata, K. Kaneda, M. Ikematsu and T. Ohsaka, *J. Energy Chem.*, 2015, **24**, 178-184.
22. M. I. Awad, M. M. Saleh and T. Ohsaka, *J. Electrochem. Soc.*, 2006, **153**, D207.
23. M. I. Awad, S. Sata, K. Kaneda, M. Ikematsu, T. Okajima and T. Ohsaka, *Electrochem. Commun.*, 2006, **8**, 1263-1269.
24. F. Okada and K. Naya, *J. Electrochem. Soc.*, 2009, **156**, E125.
25. H. Cai, Y. Sun, X. Zhang, L. Zhang, H. Liu, Q. Li, T. Bo, D. Zhou, C. Wang and J. Lian, *Materials (Basel)*, 2019, **12**.
26. D. J. Cant, K. L. Syres, P. J. Lunt, H. Radtke, J. Treacy, P. J. Thomas, E. A.

Lewis, S. J. Haigh, P. O'Brien, K. Schulte, F. Bondino, E. Magnano and W. R. Flavell, *Langmuir*, 2015, **31**, 1445-1453.

27. M. Acik, I. K. Park, R. E. Koritala, G. Lee and R. A. Rosenberg, *J. Mater. Chem. A.*, 2018, **6**, 1423-1442.
28. D. A. Zatsepin, D. W. Boukhvalov, N. V. Gavrilov, E. Z. Kurmaev, A. F. Zatsepin, L. Cui, V. Y. Shur and A. A. Esin, *Appl. Surf. Sci.*, 2017, **405**, 129-136.